AAS 26-622

QUASI-PERIODIC INVARIANT MANIFOLDS IN THE IN-PLANE QUASI-HILL RESTRICTED FOUR-BODY PROBLEM

Guido Grossi,* Nicola Baresi,† Francesco Topputo‡

The In-plane Quasi-Hill Restricted Four-Body Problem (IQHR4BP) is a quasi-periodic dynamical model tailored to investigate motion within the Earth–Moon system. It extends the CR3BP by incorporating two periodic perturbations: solar gravity, via the Hill approximation, and Earth–Moon pulsation. This paper presents a numerical methodology, based on pseudo-arclength continuation, to transition periodic orbits from the CR3BP into three-dimensional invariant tori within the IQHR4BP. The continuation path bridges these dynamical regimes by first scaling the solar perturbation to compute two-dimensional tori in the Hill-Restricted Four-Body Problem (HR4BP), and subsequently introducing lunar eccentricity to reach the IQHR4BP. The core algorithm iteratively solves a two-point boundary value problem for the invariant surface of a stroboscopic map. To overcome the extreme dimensionality and numerical sensitivities inherent to high-order tori, a dual-layer adaptive correction strategy is introduced. The framework actively couples adaptive pseudo-spectral collocation for trajectory propagation with dynamic spectral resolution adjustment for the Fourier representation of the invariant sections. The resulting pipeline provides a robust numerical architecture to bridge the gap between simplified astrodynamical models and high-fidelity quasi-periodic dynamics.

INTRODUCTION

Numerous astrodynamical models have been developed to describe spacecraft motion within the Sun–Earth–Moon (SEM) system. Hierarchical studies indicate that lunar eccentricity and solar gravitational perturbations constitute the most critical effects to incorporate when extending beyond the Earth–Moon Circular Restricted Three-Body Problem (CR3BP).[1–3] Traditionally, Earth–Moon pulsation is introduced through the Elliptic Restricted Three-Body Problem (ER3BP),[4] while solar perturbations are often included in a non-coherent manner via the Bicircular Restricted Four-Body Problem (BR4BP).[5] These two effects have also been combined in the Elliptic-Circular Restricted Four-Body Problem (ECR4BP) to account for both perturbations simultaneously.[6] Alternatively, a coherent formulation introduces the Sun through Hill's approximations, leading to the Hill Restricted Four-Body Problem (HR4BP),[7,8] with lunar eccentricity subsequently incorporated to form the In-plane Quasi-Hill Restricted Four-Body Problem (IQHR4BP).[9] Recent investigations have demonstrated that the IQHR4BP provides a high-fidelity surrogate for full-ephemeris models, exhibiting strong agreement in terms of trajectory propagation.[10–14]

Despite its fidelity, effectively navigating the phase space of the IQHR4BP remains a challenging task. Periodic orbits (POs) of the CR3BP are expected to evolve into two-dimensional quasi-periodic orbits (QPOs) in the HR4BP, and ultimately into three-dimensional QPOs within the IQHR4BP.[15] However, tracking this transition through model continuation is numerically demanding. A major source of difficulty lies in the need to handle three-dimensional invariant tori along the continuation path. Numerical methods in this context strongly depend on the accuracy of the torus parameterization; yet during continuation these manifolds may become highly distorted, making their representation increasingly delicate. In particular, the discretization

*Ph.D. student, Department of Aerospace Science and Technology, Politecnico di Milano, via La Masa 34, 20156 Milan, Italy
†Senior Lecturer, Surrey Space Centre, University of Surrey, Guildford GU2 7XH, United Kingdom
‡Full Professor, Department of Aerospace Science and Technology, Politecnico di Milano, via La Masa 34, 20156 Milan, Italy

of the torus plays a critical role in the convergence of the numerical scheme, while the rapid growth in the number of variables severely limits the scalability of the computation.[11,16,17]

The present work addresses these challenges by proposing a continuation strategy designed to bridge simplified and high-fidelity dynamical models. The proposed methodology builds upon the solution of a two-point boundary value problem for the invariant curves of a stroboscopic map, known in the literature as the GMOS algorithm.[18–20] The formulation incorporates a dual-layer correction strategy: an adaptive collocation scheme governing trajectory propagation,[16,21,22] together with a spectral resolution adjustment for the accurate representation of invariant sections of the stroboscopic map.[18,19,23,24] In this framework, the parameterization of the invariant manifold is dynamic and adapts to the evolving geometry of the torus during continuation. The robustness of the pipeline is demonstrated through a systematic transition from one-dimensional POs to three-dimensional invariant tori, achieved first by gradually introducing solar perturbations and subsequently by increasing the lunar eccentricity.

The outcome of this process is a parameterized representation of the invariant torus in terms of three angular variables. Two of these angles correspond to the forcing terms of the IQHR4BP, associated with the phases of the synodic and anomalistic months.[10,25] This representation naturally leads to the construction of torus maps, which constitute a valuable tool for mission design, as they allow for the direct extraction and visualization of key orbital parameters and dynamical quantities. Such tools have already proven instrumental for complex trajectory design tasks, including eclipse avoidance strategies,[6,26,27] formation-flight configurations,[28] and loitering architectures on QPOs.[13] Moreover, they provide informed initial guesses for the final transition to full-ephemeris trajectory models.[29] In this perspective, given the close dynamical similarity between the IQHR4BP and full-ephemeris formulations, the present work contributes an additional building block toward a hierarchical mission design framework, enabling dynamical structures identified in simplified models to be progressively lifted to higher-fidelity dynamics while preserving their underlying characteristics.

BACKGROUND

This section introduces the dynamical models of the Earth–Moon system, alongside the theoretical framework for quasi-periodic invariant tori. We first define the common nomenclature adopted throughout this work. The subscripts S, E, M, and B denote the Sun, Earth, Moon, and the Earth–Moon barycenter, respectively. The mass and the dimensional standard gravitational parameter of a generic body i are indicated by M_i and $\tilde{\mu}_i$, respectively. The dimensional time, measured in seconds, is denoted by t, and differentiation with respect to t is indicated by $\dot{(\cdot)}$.

Sun–Earth–Moon Hill Three-Body Problem

The Hill Three-Body Problem (H3BP), originally formulated by George William Hill in 1878 as part of his seminal work on lunar theory,[30] provides a local approximation of the motion of three point masses under their mutual gravitational attraction. It describes a system in which one body is significantly more massive than the other two, while the latter remain relatively close to each other and far from the dominant primary. Hill's assumptions are well satisfied by the SEM system, where $M_\mathrm{S} \gg M_\mathrm{E}$ and $M_\mathrm{S} \gg M_\mathrm{M}$. This hierarchy is quantified by the mass parameter $\mu_{\mathrm{B,S}} = (\tilde{\mu}_\mathrm{E} + \tilde{\mu}_\mathrm{M})/\tilde{\mu}_\mathrm{S} \approx 3.0404 \times 10^{-6} \ll 1$.

The model can be derived either by applying a change of coordinates to the general three-body equations of motion and taking the limit $\mu_{\mathrm{B,S}} \to 0$, while expanding the resulting equations and retaining only first-order terms in $\mu_{\mathrm{B,S}}$, or equivalently by considering it as a limiting case of the CR3BP.[4] In this limiting process, the gravitational potential of the primary is expanded about the secondary, and only the leading-order tidal contribution (quadratic in the distance from the secondary) is retained. As a result, the primary is effectively moved to infinity, and its gravitational influence is reduced to a uniform tidal field.

As noted by Hénon,[31] the mass ratio between the two smaller interacting bodies may be arbitrary, provided that their combined mass remains infinitesimal relative to the dominant primary. Consequently, the Hill formulation naturally encompasses the restricted case, in which the mass of the third body is negligible compared to that of the secondary.

An additional assumption is that the Earth–Moon barycenter follows a circular mean orbit about the Sun. As shown by Scheeres,[8] this approximation is consistent with the retained order of accuracy provided that the actual orbital eccentricity satisfies $e = \mathcal{O}(\mu_{\mathrm{B,S}}^{1/3})$. For the SEM system, the Earth's orbital eccentricity is $e_{\mathrm{EM}} \approx 0.0167$, which is in close agreement with $\mu_{\mathrm{B,S}}^{1/3} \approx 0.0145$. Under these assumptions, the resulting model is referred to as the circular Hill problem, although its elliptic counterpart has also been studied in the literature.[32]

To describe the dynamics, a rotating, right-handed Cartesian frame, referred to as Hill's frame and denoted by $\mathcal{H}$, is introduced. Its basis vectors are $(\hat{\mathbf{i}}_{\mathcal{H}}, \hat{\mathbf{j}}_{\mathcal{H}}, \hat{\mathbf{k}}_{\mathcal{H}})$. The frame is centered at the secondary (the Earth) and rotates about the inertially fixed axis $\hat{\mathbf{k}}_{\mathcal{H}}$ with an angular velocity $\Omega_{\mathcal{H}}$ equal to the mean motion of the Earth–Moon barycenter around the Sun. The Sun–Earth line defines the $\hat{\mathbf{i}}_{\mathcal{H}}$ direction, the $\hat{\mathbf{k}}_{\mathcal{H}}$ axis is orthogonal to the ecliptic plane, and $\hat{\mathbf{j}}_{\mathcal{H}}$ completes the right-handed triad. The frame is shown in Figure 1.

The system is strictly nondimensionalized to obtain equations of motion that are free of explicit parameters. The characteristic length is chosen as the Hill radius, $\mathrm{LU}_{\mathcal{H}} = l_{\mathrm{SB}}\, \mu_{\mathrm{B,S}}^{1/3}$, where l_{SB} is the mean distance between the Sun and the Earth–Moon barycenter, taken as 1 AU. The characteristic time is defined as the inverse of the mean motion of the Earth–Moon barycenter about the Sun, $\mathrm{TU}_{\mathcal{H}} = \sqrt{l_{\mathrm{SB}}^3/\tilde{\mu}_{\mathrm{S}}}$, yielding the nondimensional time variable $t_{\mathcal{H}} = t/\mathrm{TU}_{\mathcal{H}}$. Derivatives with respect to $t_{\mathcal{H}}$ are denoted by $\overset{\star}{(\cdot)}$ and satisfy $\overset{\star}{(\cdot)} = \dot{(\cdot)}\,\mathrm{TU}_{\mathcal{H}}$. Under this scaling, one revolution of the Earth–Moon barycenter around the Sun corresponds to a nondimensional period of 2π, and the angular velocity of the Hill frame becomes $\Omega_{\mathcal{H}} = 1\ \mathrm{rad}/\mathrm{TU}_{\mathcal{H}}$. Furthermore, the adopted normalization places the Sun at $\mathbf{r}_{\mathrm{S}} = -\mu_{\mathrm{B,S}}^{-1/3}\hat{\mathbf{i}}_{\mathcal{H}}$. The autonomous Hill's equations of motion and the associated Jacobi constant are provided in Appendix A.

A particular planar prograde periodic solution of Eq. (33) is known as the Hill's Variational Orbit (HVO). This orbit, represented in Figure 1, was originally found by Hill as a periodic solution whose period corresponds to one synodic month, thereby providing a first representation of the actual Moon.[33,34] The orbit belongs to a one-parameter family of periodic solutions, commonly referred to as the variational orbit family (later classified as "family g" by Hénon[35]), which is parameterized by a single parameter m. Within this family, the HVO is obtained for $m = m_{\mathrm{SEM}} \approx 0.08085$ which corresponds to the ratio between the synodic month (approximately 29.53 days) and one sidereal year (≈ 365.25 days). The orbital period is $2\pi m_{\mathrm{SEM}}$ measured in $\mathrm{TU}_{\mathcal{H}}$.

Despite its historical relevance, the HVO is strictly planar and confined to the ecliptic plane, and therefore does not capture the inclination of the lunar orbit and the associated draconic month. Moreover, being strictly periodic with a fixed geometry, it does not reproduce the actual Earth–Moon distance variation, and thus neglects the orbital eccentricity and the associated anomalistic month. These limitations motivate the transition toward quasi-periodic representations of the lunar motion. By relaxing the strictly periodic structure of the HVO, one obtains quasi-periodic solutions, such as the Quasi-Hill's Variational Orbit (QHVO) illustrated in Figure 1. The construction and specific role of this extended orbit will be detailed in the subsequent sections.

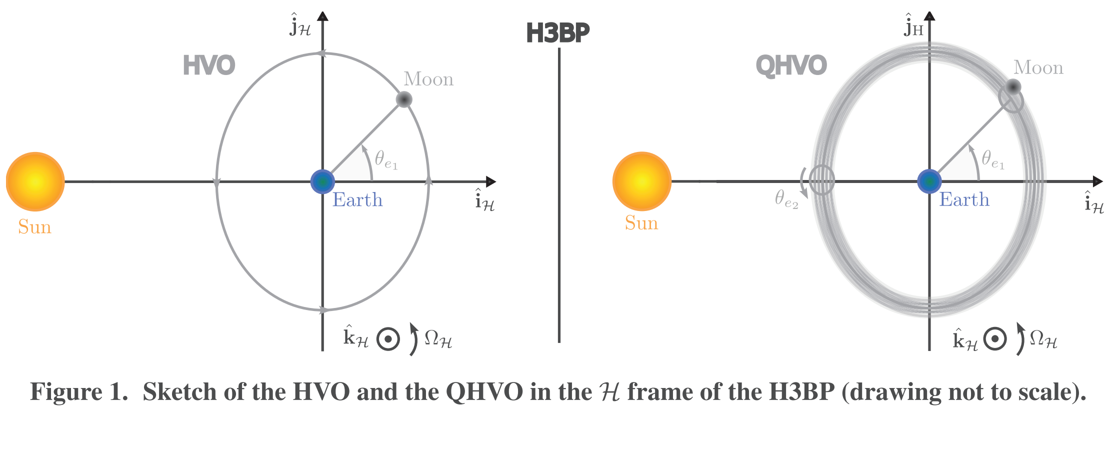

Figure 1. Sketch of the HVO and the QHVO in the $\mathcal{H}$ frame of the H3BP (drawing not to scale).

Hill-Restricted Four-Body Problem

The HR4BP is a natural extension of the H3BP, in which a fourth, infinitesimal-mass body (e.g., a spacecraft) is introduced into the Hill framework. Under the restricted assumption, the spacecraft does not affect the motion of the primaries, and the Earth–Moon dynamics remains governed by Eq. (33), independently of the spacecraft motion. Within this setting, any solution of the H3BP can be prescribed for the Earth–Moon motion. The spacecraft dynamics is then obtained by considering its motion in the time-dependent gravitational field generated by this prescribed solution $\mathbf{r}_{\text{EM}}(t)$. This construction makes the model highly flexible and allows for the definition of more general dynamical variants. In its original formulation, Scheeres selected the HVO to represent the Earth–Moon motion, leading to the SEM HR4BP.[8] In this case, the resulting dynamics inherits the dependence on the parameter m. In the limit $m \to 0$, the distance to Sun increases, and its influence becomes negligible, recovering the CR3BP.

Also in this case, the dynamics are recast in a uniformly rotating frame centered at the Earth–Moon barycenter (EMB), hereafter referred to as Scheeres' frame and denoted by $\mathcal{S}$. The Cartesian axes $(\hat{\mathbf{i}}_{\mathcal{S}}, \hat{\mathbf{j}}_{\mathcal{S}}, \hat{\mathbf{k}}_{\mathcal{S}})$ are defined such that $\hat{\mathbf{k}}_{\mathcal{S}}$ is parallel to $\hat{\mathbf{k}}_{\mathcal{H}}$, while $\hat{\mathbf{i}}_{\mathcal{S}}$ rotates within the Sun–Earth plane. The unit vector $\hat{\mathbf{j}}_{\mathcal{S}}$ completes the right-handed orthonormal triad.

The nondimensionalization differs from that of the H3BP. The length unit is chosen as the mean Earth–Moon distance associated with the HVO. It is defined as $\text{LU}_{\mathcal{S}}(m) = a_0(m)\, l_{\text{SB}}\, \mu_{\text{B,S}}^{1/3} = a_0(m)\, \text{LU}_{\mathcal{H}}$, where $a_0(m)$ is a function of m, expressible as a power series. In this work, the coefficients provided in Appendix A of Reference 36 are adopted. The time unit is $\text{TU}_{\mathcal{S}}(m) = 1/m\sqrt{l_{\text{SB}}^3/\tilde{\mu}_{\text{S}}} = \text{TU}_{\mathcal{H}}/m$. The constant angular velocity of the rotating frame is $\Omega_{\mathcal{S}} = (1+m)$ rad/$\text{TU}_{\mathcal{S}}$. Both the length and time scales depend on m, which plays a central role in the continuation from $m = 0$ to $m = m_{\text{SEM}}$. Derivatives with respect to the nondimensional time $t_{\mathcal{S}}$ are denoted by $\mathring{(\cdot)}$ and satisfy $\mathrm{d}(\cdot)/\mathrm{d}t_{\mathcal{S}} = \mathring{(\cdot)} = \dot{(\cdot)}\,\text{TU}_{\mathcal{S}} = 1/m\,\overset{\star}{(\cdot)}$. For $m = m_{\text{SEM}}$, one period $2\pi\,\text{TU}_{\mathcal{S}}$ corresponds to one synodic month.

The positions of the Earth and the Moon with respect to the EMB are $\mathbf{r}_{\text{E}} = -\mu_{\text{M,B}}\,\mathbf{r}_{\text{EM}}$ and $\mathbf{r}_{\text{M}} = (1-\mu_{\text{M,B}})\,\mathbf{r}_{\text{EM}}$, respectively, and $\mu_{\text{M,B}} = \tilde{\mu}_{\text{M}}/(\tilde{\mu}_{\text{M}} + \tilde{\mu}_{\text{E}}) \approx 0.01215$ is the mass parameter of the Earth–Moon system. Since the Earth–Moon motion is prescribed by the selected solution of the H3BP, neither body is stationary in the $\mathcal{S}$ frame; instead, both oscillate periodically about their mean positions. The Sun follows a circular motion about the EMB and is located at

$$\boldsymbol{\rho}_{\text{S}}(t_{\mathcal{S}}) = \mu_{\text{B,S}}^{-1/3}\, a_0(m)\, (-\cos(t_{\mathcal{S}} + t_{\mathcal{S},0})\,\hat{\mathbf{i}}_{\mathcal{S}} + \sin(t_{\mathcal{S}} + t_{\mathcal{S},0})\,\hat{\mathbf{j}}_{\mathcal{S}}).$$

Without loss of generality, we set $t_{\mathcal{S},0} = 0$, such that at $t_{\mathcal{S}} = 0$ the Sun, Earth, and Moon are aligned in a Sun–Earth–Moon syzygy along the $\hat{\mathbf{i}}_{\mathcal{S}}$ axis (full Moon configuration). A schematic representation of the model is shown in Figure 2.

Let $\mathbf{r} = [x, y, z]^\top$ and $\mathbf{v} = [\mathring{x}, \mathring{y}, \mathring{z}]^\top$ denote the nondimensional position and velocity of the spacecraft in the $\mathcal{S}$ frame, respectively, and define the state vector as $\mathbf{x} = [\mathbf{r}^\top, \mathbf{v}^\top]^\top \in \mathbb{R}^6$. The dynamics of the HR4BP is described by the following system of first-order differential equations:

$$\mathring{\mathbf{x}} = \mathbf{f}(\mathbf{x}, t_{\mathcal{S}}), \tag{1}$$

where $\mathbf{f}$ represents the time-periodic vector field of the model. The complete formulation of the equations of motion is provided in Appendix B.

Overall, the HR4BP is a time-periodic Hamiltonian system whose minimal period is $\pi\,\text{TU}_{\mathcal{S}}$, corresponding to half a synodic month when $m = m_{\text{SEM}}$. The model may be viewed as a periodically forced Earth–Moon CR3BP, where the perturbation induced by the Sun is π-periodic. This half-periodicity arises from the symmetries inherited from both the Hill approximation and the HVO. In particular, the solar tidal field is symmetric with respect to the Earth–Moon barycenter, while the variational orbit is invariant under a half-period rotation in the $\mathcal{S}$ frame.

Considerable effort has been devoted to characterizing the dynamics of the HR4BP, identifying families of periodic and quasi-periodic orbits, together with their associated invariant manifolds.[13,23,24,36–42]

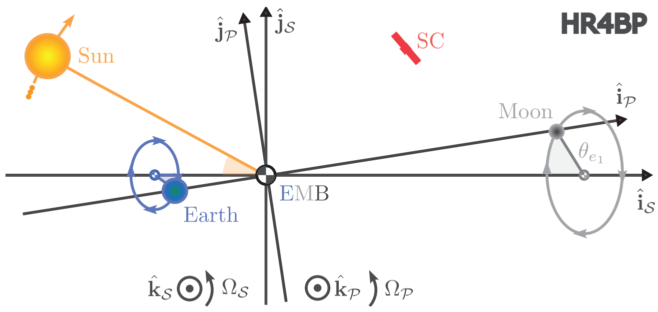

Figure 2. Sketch of the HR4BP in the $\mathcal{S}$ frame (drawing not to scale).

As the subsequent developments of this work focus specifically on the computation and parameterization of quasi-periodic invariant tori, it is convenient to recast the non-autonomous dynamics as an equivalent extended autonomous system. This is achieved by replacing the time variable $t_{\mathcal{S}} \in \mathbb{R}$ with the external phase $\theta_{e_1} \in \mathbb{T} := \mathbb{R}/(2\pi\mathbb{Z})$, defined as $\theta_{e_1}(t_{\mathcal{S}}) = \omega_{e_1} t_{\mathcal{S}} + \theta_{e_1,0} \pmod{2\pi}$, where $\theta_{e_1,0}$ represents the initial phase of the periodic forcing. This formulation introduces the external phase as an additional state variable, while allowing different initial configurations of the time-dependent environment to be considered through the parameter $\theta_{e_1,0}$. Although the initial time is fixed at $t_{\mathcal{S}} = 0$, the introduction of $\theta_{e_1,0}$ provides an additional degree of freedom that is particularly useful in the continuation framework, where the initial phase can be adjusted to follow solution families and ensure a consistent transition between different dynamical models. Since the forcing is π-periodic, the external frequency is $\omega_e = 2$ rad/TU$_{\mathcal{S}}$, corresponding to an external period $T_e = \pi$ TU$_{\mathcal{S}}$. The resulting extended system is:

$$\begin{cases} \mathring{\mathbf{x}} = \mathbf{f}(\mathbf{x}, \theta_{e_1}) \\ \mathring{\theta}_{e_1} = \omega_{e_1} \end{cases} . \tag{2}$$

In-Plane Quasi-Hill-Restricted Four-Body Problem

The IQHR4BP is a quasi-periodic extension of the HR4BP that incorporates the Earth–Moon distance variation (pulsation) while preserving the Hill framework.[9,10] This is achieved by replacing the periodic HVO with a planar QHVO, obtained by exciting the in-plane center manifold of the HVO. The linear stability of the HVO reveals the existence of two center manifolds: an in-plane manifold and an out-of-plane manifold. Interestingly, the characteristic periods associated with these center directions are numerically close to the anomalistic and draconic months of the real Earth–Moon system, respectively, as observed by Aydin[25] and exploited by Park.[9,10] This remarkable correspondence highlights the ability of Hill's approximation to accurately reproduce the dominant time scales of the real Earth–Moon dynamics, confirming the enduring relevance of Hill's lunar theory.[30,43] Continuation along the in-plane center manifold generates a family of two-dimensional QPOs. The actual QHVO is then identified as the member of this family whose eccentricity matches that of the Earth–Moon orbit, namely $e_{\text{EM}} \approx 0.055$. A sketch of the QHVO is shown in Figure 1.

For consistency, the motion of the spacecraft is described in the same $\mathcal{S}$ frame as the HR4BP and using the same nondimensional units. In this way, Eqs. (35) and (36) still apply, with the only difference that $\mathbf{r}_{\text{EM}}$ is no longer given by Eq. (37), but is instead prescribed by the QHVO. The resulting QHVO depends on two angular variables, $\boldsymbol{\theta}_e = [\theta_{e_1}, \theta_{e_2}]^\top$, evolving with frequencies $\boldsymbol{\omega}_e = [\omega_{e_1}, \omega_{e_2}]^\top$. These frequencies correspond to the synodic lunar month and the anomalistic lunar month (≈ 27.56 days), respectively. The angle θ_{e_1} governs the longitudinal motion on the underlying HVO, as in the HR4BP, while θ_{e_2} governs the latitudinal modulation. A schematic representation of the IQHR4BP is shown in Figure 3. The resulting dynamical model is therefore a quasi-periodic Hamiltonian system, which can be written as:

$$\begin{cases} \mathring{\mathbf{x}} = \mathbf{f}(\mathbf{x}, \boldsymbol{\theta}_e) \\ \mathring{\boldsymbol{\theta}}_e = \boldsymbol{\omega}_e \end{cases} . \tag{3}$$

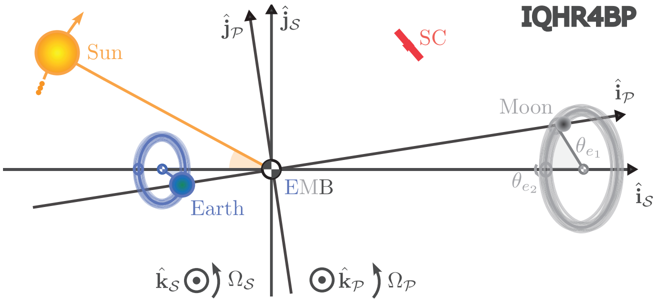

Figure 3. Sketch of the IQHR4BP in the $\mathcal{S}$ frame (drawing not to scale).

Rotating–Pulsating Frame

For the sake of comparing orbits across different dynamical models, it is convenient to define a frame that both rotates and pulsates with the Earth and the Moon, such that the two bodies occupy fixed positions in this reference frame.[1] This frame is known as the rotating–pulsating frame and is denoted, in the remainder of the paper, by $\mathcal{P}$. Its origin is located at the Earth–Moon barycenter. The unit vector $\hat{\mathbf{i}}_\mathcal{P}$ is always directed from the Earth to the Moon, while $\hat{\mathbf{k}}_\mathcal{P}$ is orthogonal to the instantaneous Earth–Moon orbital plane, and $\hat{\mathbf{j}}_\mathcal{P}$ completes the right-handed orthonormal triad. The transformations between the $\mathcal{H}$, $\mathcal{S}$, and $\mathcal{P}$ frames can be found in Reference 9. A constant time unit is defined as $\mathrm{TU}_\mathcal{P} = \sqrt{(\tilde{\mu}_\mathrm{E} + \tilde{\mu}_\mathrm{M})/l^3_\mathrm{EM}}$, where $l_\mathrm{EM} = 384\,400$ km. The time-dependent length unit is defined as the instantaneous Earth–Moon distance, $\mathrm{LU}_\mathcal{P}(t_\mathcal{P}) = \|\mathbf{R}_\mathrm{EM}(t_\mathcal{P})\|$, where $\mathbf{R}_\mathrm{EM}(t)$ is the dimensional Earth–Moon relative position vector in any reference frame. The rotating–pulsating frame is employed to represent orbits of the HR4BP or IQHR4BP (see Figures 2 and 3).

Invariant Tori

Several theoretical frameworks have been developed to understand quasi-periodic motion in dynamical systems, particularly Hamiltonian ones. Among the most influential is the Kolmogorov–Arnold–Moser (KAM) theory, which addresses the persistence of invariant tori under sufficiently small perturbations. The objective of this work, however, is not to study the existence of such solutions, but rather to compute, continue, and characterize them in order to assess their potential for spacecraft trajectory design, following recent efforts to extend mission design techniques beyond periodic orbits.[21,44–47] The remainder of this section sets the notation and recalls the concepts most relevant to the developments presented herein.

A D-dimensional invariant torus $\mathcal{T} \subset \mathbb{R}^6$ is an invariant manifold parameterized by D angular variables $\boldsymbol{\theta} = [\theta_1, \ldots, \theta_D]^\top \in \mathbb{T}^D$, on which the flow is diffeomorphic to a linear flow $\dot{\boldsymbol{\theta}} = \boldsymbol{\omega}$, with frequency vector $\boldsymbol{\omega} = [\omega_1, \ldots, \omega_D]^\top$. The diffeomorphism $\boldsymbol{\tau} : \mathbb{T}^D \to \mathcal{T} \subset \mathbb{R}^6$ mapping angle space to phase space (the state space) is called the torus function and satisfies the invariance equation[47]

$$\boldsymbol{\varphi}(\boldsymbol{\tau}(\boldsymbol{\theta}), t) = \boldsymbol{\tau}(\boldsymbol{\theta} + \boldsymbol{\omega} t), \tag{4}$$

where $\boldsymbol{\varphi}(\cdot, t)$ denotes the flow induced by the vector field $\mathbf{f}$. By differentiating Eq. (4) with respect to time and evaluating it at $t = 0$, one can obtain the infinitesimal version of the invariance equation:

$$\mathbf{f}(\boldsymbol{\tau}(\boldsymbol{\theta}), 0) = \frac{\partial \boldsymbol{\tau}(\boldsymbol{\theta})}{\partial \boldsymbol{\theta}} \boldsymbol{\omega}. \tag{5}$$

Geometrically, this condition requires that at any point $\boldsymbol{\tau}(\boldsymbol{\theta})$, the vector field $\mathbf{f}$ must be tangent to the manifold. This means the local time derivative of the dynamics must lie entirely within the local tangent space of the torus, which is spanned by the columns of the Jacobian matrix $\partial \boldsymbol{\tau}/\partial \boldsymbol{\theta}$. The torus function therefore provides a parameterization of the invariant manifold, and evolving a trajectory on the torus is equivalent to a rigid translation of the angle variables. Trajectories lying on an invariant torus are referred to as QPOs. Figure 4 illustrates a standard torus in the angle space and an invariant torus in the phase space.

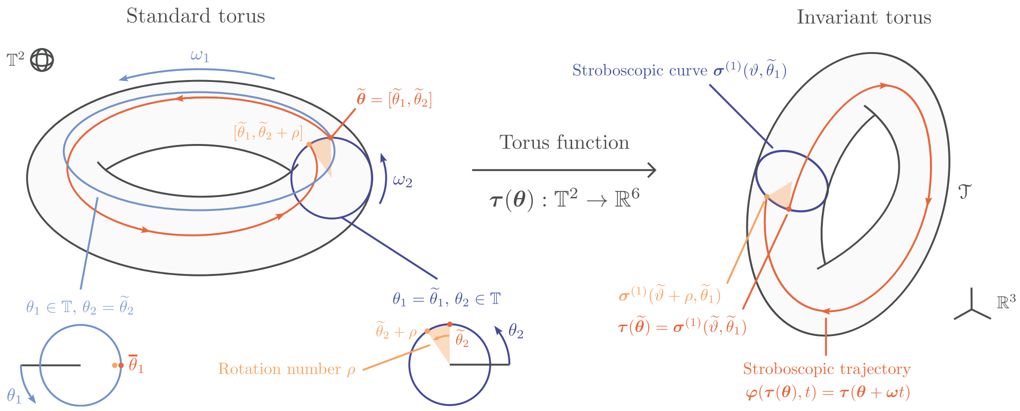

Figure 4. Illustration of a standard two-torus (left) and a two-dimensional invariant torus (right) mapped by the torus function; a trajectory propagated for one stroboscopic period is shown on both manifolds.

When dealing with non-autonomous systems, the angles and frequencies are partitioned into internal $(\boldsymbol{\theta}_i, \boldsymbol{\omega}_i)$ and external $(\boldsymbol{\theta}_e, \boldsymbol{\omega}_e)$ components, structuring the vectors as $\boldsymbol{\theta} = [\boldsymbol{\theta}_i^\top, \boldsymbol{\theta}_e^\top]^\top, \quad \boldsymbol{\omega} = [\boldsymbol{\omega}_i^\top, \boldsymbol{\omega}_e^\top]^\top$. Internal frequencies arise from the intrinsic dynamics of the system (e.g., periodic orbits in the CR3BP), whereas external frequencies are imposed by time-periodic or quasi-periodic forcing. For an n-degree-of-freedom Hamiltonian system with D_e external frequencies, the torus dimension satisfies $D_e \leq D \leq D_e + n$, or equivalently $D_i = D - D_e \leq n$. Invariant tori typically belong to D_i-parameter Cantor families.[18] Throughout this work, all frequency vectors are assumed to be incommensurate, and the dynamical models considered here fit naturally within this framework. Periodic orbits of the CR3BP and H3BP are one-dimensional tori ($D = 1$, $D_i = 1$, $D_e = 0$). The QHVO is a two-dimensional torus ($D = 2$, $D_i = 2$, $D_e = 0$). Non-resonant CR3BP periodic orbits continued into the HR4BP become two-dimensional tori ($D = 2$, $D_i = 1$, $D_e = 1$), whereas those of the IQHR4BP are three-dimensional tori ($D = 3$, $D_i = 1$, $D_e = 2$). When a torus is continued between different models (e.g., CR3BP $\to$ HR4BP $\to$ IQHR4BP), we refer to this as external continuation. Instead, continuation within the same model (e.g., HVO $\to$ QHVO) is referred to as internal continuation.

For computational purposes, it is convenient to introduce the stroboscopic map, where $T_s = 2\pi/\omega_s$ is the stroboscopic period associated with the stroboscopic frequency ω_s, corresponding to the s-th component of the frequency vector $\boldsymbol{\omega}$ (with $1 \leq s \leq D$). Under the map $\boldsymbol{\varphi}(\cdot, T_s)$, the stroboscopic angle θ_s returns to its initial value modulo 2π. As a result, instead of computing the full D-dimensional manifold, one can concentrate on its $(D-1)$-dimensional intersection with the surface of section $\theta_s = \widetilde{\theta}_s$ defined in the torus angle space $\mathbb{T}^D$. Let $\boldsymbol{\vartheta}^{(s)} \in \mathbb{T}^{D-1}$ and $\boldsymbol{\mathrm{\omega}}^{(s)} \in \mathbb{R}^{D-1}$ denote the angle and frequency vectors obtained by removing the s-th components of $\boldsymbol{\theta}$ and $\boldsymbol{\omega}$, respectively. These are referred to as the reduced angles and reduced frequencies, and they can still be partitioned into external and internal components. The associated rotation vector $\boldsymbol{\rho}^{(s)} \in \mathbb{R}^{(D-1)}$ is

$$\boldsymbol{\rho}^{(s)} = \boldsymbol{\mathrm{\omega}}^{(s)} T_s, \tag{6}$$

which represents the angular displacement of the reduced angles after one stroboscopic period.

The stroboscopic torus function, $\boldsymbol{\sigma}^{(s)} : \mathbb{T}^{D-1} \times \mathbb{T} \to \mathcal{T} \subset \mathbb{R}^6$, parameterizes the stroboscopic section $\Sigma^{(s, \widetilde{\theta}_s)}$ obtained by fixing the s-th angular coordinate θ_s to $\widetilde{\theta}_s$ on the invariant torus $\mathcal{T}$. Each value of θ_s therefore defines a distinct stroboscopic section of the torus. The invariance condition Eq. (4) specializes to

$$\boldsymbol{\varphi}(\boldsymbol{\sigma}(\boldsymbol{\vartheta}, \theta_s), T_s) = \boldsymbol{\sigma}(\boldsymbol{\vartheta} + \boldsymbol{\mathrm{\omega}} T_s, \theta_s + \omega_s T_s) = \boldsymbol{\sigma}(\boldsymbol{\vartheta} + \boldsymbol{\rho}, \theta_s), \tag{7}$$

where the superscript (s) is omitted to simplify the notation.

Since the stroboscopic period T_s is generally unknown and must be determined as part of the solution, it is convenient to normalize the independent variable by introducing the normalized stroboscopic time $\tau = t/T_s$, where t denotes the independent variable of the underlying dynamical model (e.g., $t_{\mathcal{H}}$ or $t_{\mathcal{S}}$). Over one stroboscopic period, the normalized time varies from 0 to 1. Derivatives with respect to τ are denoted by $(\cdot)'$ and satisfy $\mathrm{d}(\cdot)/\mathrm{d}\tau = (\cdot)' = T_s\, \mathrm{d}(\cdot)/\mathrm{d}t$. Accordingly, a dynamical system of the form $\mathrm{d}\mathbf{x}/\mathrm{d}t = \mathbf{f}(\mathbf{x}, t)$ can be equivalently written

$$\mathbf{x}' = T_s\, \widetilde{\mathbf{f}}(\mathbf{x}, \tau). \tag{8}$$

Unfolding Parameters

Unfolding parameters $\boldsymbol{\lambda} \in \mathbb{R}^{D_i}$ are introduced to augment the system dynamics, unfolding the degeneracies associated with the invariants of motion $\boldsymbol{I}(\mathbf{x}, \tau)$.[48,49] The primary advantage of adding a number of unfolding parameters equal to the intrinsic dimension D_i of the torus is squaring the otherwise non-square Jacobian matrix of the Newton-Raphson collocation algorithm. This circumvents the need for computationally expensive routines (e.g., QR factorization), leading to a much faster solution of the linear system while rendering the continuation algorithms significantly more robust against dynamical and numerical instabilities.

These parameters are embedded into the augmented vector field in such a way that a valid physical solution to the original system is found if and only if $\boldsymbol{\lambda} = \mathbf{0}$. Specifically, the Jacobi constant is used to augment the dynamics in autonomous models, whereas the local actions of the torus, which locally behave similarly to integrals of motion, are employed for non-autonomous systems.[21] The resulting augmented vector field is expressed as

$$\boldsymbol{f}(\mathbf{x}, \tau, \boldsymbol{\lambda}) = T_s\, \widetilde{\mathbf{f}}(\mathbf{x}, \tau) + \left(\frac{\partial \boldsymbol{I}}{\partial \mathbf{x}}\right)^{\top} \boldsymbol{\lambda}, \tag{9}$$

which perfectly matches the original, unperturbed vector field when $\boldsymbol{\lambda} = \mathbf{0}$.

METHODOLOGY

This section outlines the numerical methodology developed in this work. First, the discretization and computation of invariant tori are formulated, followed by the introduction of the dual-layer adaptive strategy for error control. Finally, the pseudo-arclength continuation framework and the nonlinear solution process are detailed, outlining the transition across three continuation phases: internal continuation within the H3BP, and external continuations from the CR3BP to the HR4BP, and ultimately to the IQHR4BP.

Discretization of Invariant Tori

In this work, invariant tori are computed using a fully numerical approach. Compared to analytical methods, numerical ones are less model-dependent and are well suited for the continuation of families of QPOs, as they typically require minimal modifications beyond updating the force field.[16,50]

To compute invariant tori, a two-point boundary value problem is formulated to determine the invariant surface of a stroboscopic map associated with a D-dimensional torus.[19,20] Rather than relying on numerical integration of the dynamics, pseudospectral collocation is used to propagate the states of the stroboscopic section under the stroboscopic map. The collocation scheme for such a problem was first described by Olikara.[21] In the present work, we expand the formulation by incorporating two levels of correction for the two parameterizations involved in the computation of the stroboscopic section. The first deals with the points used to parameterize the invariant section itself, and the second controls the quasi-periodic trajectories generated by the flow.

Fourier Discretization By definition, a D-dimensional torus function $\boldsymbol{\tau}(\boldsymbol{\theta})$ is periodic in each of its arguments. Within a numerical framework, it is therefore natural to approximate it via a multidimensional discrete Fourier transform as

$$\boldsymbol{\tau}(\boldsymbol{\theta}) = \sum_{\boldsymbol{j} \in \mathbb{Z}^D} \mathbf{c}_{\boldsymbol{j}}\, e^{\mathrm{i}\, \boldsymbol{j}^{\top} \boldsymbol{\theta}} \approx \sum_{\boldsymbol{j} \in \mathcal{J}_D} \mathbf{c}_{\boldsymbol{j}}\, e^{\mathrm{i}\, \boldsymbol{j}^{\top} \boldsymbol{\theta}}, \tag{10}$$

where i is the imaginary unit and the frequency index vector $\boldsymbol{j}$ belongs to the finite set

$$\mathcal{J}_D = \left\{ \boldsymbol{j} \in \mathbb{Z}^D : j_d \in \{-M_{F_d}, \ldots, M_{F_d}\},\ \forall\, d = 1, \ldots, D \right\}. \tag{11}$$

Here, M_{F_d} denotes the truncation order used to approximate each angular dimension. To evaluate the complex vectorial Fourier coefficients $\mathbf{c}_{\boldsymbol{j}} \in \mathbb{C}^6$, the torus function is sampled on an evenly spaced grid of angles $\boldsymbol{\theta}_{\boldsymbol{i}}$ of size $N_{F_1} \times \cdots \times N_{F_D}$, where $N_{F_d} = 2M_{F_d} + 1$ $(d = 1, \ldots, D)$. The grid nodes are defined as

$$\boldsymbol{\theta}_{\boldsymbol{i}} = 2\pi \left[\frac{i_1}{N_{F_1}}, \ldots, \frac{i_D}{N_{F_D}}\right]^\top, \tag{12}$$

where the grid index vector $\boldsymbol{i}$ belongs to the set

$$\mathcal{I}_D = \left\{\boldsymbol{i} \in \mathbb{Z}^D : i_d \in \{0, \ldots, N_{F_d} - 1\}, \, \forall\, d = 1, \ldots, D\right\}. \tag{13}$$

Denoting the sampled state at each grid node as $\mathbf{x}_{\boldsymbol{i}} = \boldsymbol{\tau}(\boldsymbol{\theta}_{\boldsymbol{i}})$, the Fourier coefficients can be computed via

$$\mathbf{c}_{\boldsymbol{j}} = \frac{1}{\prod\limits_{d=1}^{D} N_{F_d}} \sum_{\boldsymbol{i} \in \mathcal{I}_D} \mathbf{x}_{\boldsymbol{i}}\, e^{-\mathrm{i}\, \boldsymbol{j}^\top \boldsymbol{\theta}_{\boldsymbol{i}}}. \tag{14}$$

The derivative of the torus function with respect to the angles can be evaluated as

$$\frac{\partial \boldsymbol{\tau}(\boldsymbol{\theta})}{\partial \boldsymbol{\theta}} \approx \sum_{\boldsymbol{j} \in \mathcal{J}_D} \mathrm{i}\, \mathbf{c}_{\boldsymbol{j}} \boldsymbol{j}^\top e^{\mathrm{i}\, \boldsymbol{j}^\top \boldsymbol{\theta}}. \tag{15}$$

The previous definitions apply for the stroboscopic torus function $\boldsymbol{\sigma}^{(s)}(\boldsymbol{\vartheta}, \theta_s)$, with the only difference that the grid of angles $\boldsymbol{\vartheta}_{\boldsymbol{i}}$ and the indices $\boldsymbol{j}, \boldsymbol{i}$ are $(D-1)$-dimensional. The set of states $\mathbf{x}_{\boldsymbol{i}}$, $\boldsymbol{i} \in \mathcal{I}_{D-1}$, corresponds to the points on discrete stroboscopic invariant section $\Sigma^{(s,\theta_s)}$. The overall number of 6-dimensional states for a stroboscopic section is $\mathcal{N}_F = \prod_{d=1}^{D-1} N_{F_d}$.

Pseudospectral Collocation The stroboscopic invariance condition in Eq. (7) requires propagating the states on the stroboscopic section for one stroboscopic period. In this work, this is achieved using an adaptive pseudospectral collocation scheme, adapted from Reference 22.

The time horizon $\tau \in [0, 1]$ is partitioned into a grid of K intervals $\mathcal{K}_k = [\tau_{k-1}, \tau_k] \subseteq [0, 1]$ for $k = 1, \ldots, K$. The grid points are defined such that $0 = \tau_0 < \tau_1 < \cdots < \tau_{K-1} < \tau_K = 1$, satisfying

$$\bigcup_{k=1}^{K} \mathcal{K}_k = [0, 1], \quad \mathcal{K}_k \cap \mathcal{K}_{k+1} = \{\tau_k\}, \quad (k = 1, \ldots, K - 1).$$

The domain within each grid interval is then mapped to the computational domain $\zeta \in [-1, 1]$ via the affine transformation

$$\zeta = \zeta(\tau, \tau_{k-1}, \tau_k) = \frac{1}{\beta_k}(\tau - \overline{\beta}_k), \quad (k = 1, \ldots, K) \tag{16}$$

where $\overline{\beta}_k = (\tau_k + \tau_{k-1})/2$ is the mesh interval offset, and $\beta_k = \mathrm{d}\tau/\mathrm{d}\zeta = (\tau_k - \tau_{k-1})/2$ is the mesh interval scaling factor. With a slight abuse of notation, we denote differentiation with respect to ζ by $\dot{(\cdot)}$.

Within each interval k, the state vector $\mathbf{x}$ is approximated by a vector of six polynomials $\mathbf{P}_{\mathbf{x}}^{(k)}(\zeta)$, expressed in terms of the Lagrange basis polynomials $\ell_n^{(k)}(\zeta)$ $(n = 1, \ldots, N_k + 1)$, as

$$\mathbf{x}^{(k)}(\zeta) \approx \mathbf{P}_{\mathbf{x}}^{(k)}(\zeta) = \sum_{n=1}^{N_k+1} \ell_n^{(k)}(\zeta)\mathbf{x}_n^{(k)}, \quad \text{with} \quad \ell_n^{(k)}(\zeta) = \prod_{\substack{l=1 \\ l \neq n}}^{N_k+1} \frac{\zeta - \zeta_l^{(k)}}{\zeta_n^{(k)} - \zeta_l^{(k)}}, \tag{17}$$

where $\mathbf{x}_n^{(k)} \in \mathbb{R}^6$ denotes the state approximation at the node $\zeta_n^{(k)}$, and $\{\zeta_1^{(k)}, \ldots, \zeta_{N_k+1}^{(k)}\} \subset [-1, +1]$ is the set of $N_k + 1$ interpolation nodes for the k-th interval.

The points within each interval k are partitioned into collocated nodes (where the system dynamics are enforced), continuity nodes (used to ensure trajectory continuity at interval boundaries, e.g., $\zeta = -1$), and non-collocated nodes (used for interpolation, e.g., $\zeta = +1$), as illustrated in Figure 5. Node distributions are generally derived from Chebyshev, Legendre, or equidistant (EQU) polynomials.[51,52] The chosen collocation method dictates the total node count and boundary inclusion: (a) Gauss-type methods (CG, LG) use $N_k + 2$ nodes (N_k internal collocated, one continuity at -1, one non-collocated at $+1$); (b) Radau-type methods (CGR, LGR) use $N_k + 1$ nodes, collocating in $[-1, +1)$; and (c) Lobatto-type (CGL, LGL) or EQU methods use $N_k + 1$ nodes in $[-1, +1]$.

This paper employs the Chebyshev-Gauss (CG) method, where collocation occurs within $(-1, +1)$ and the right boundary $\zeta = +1$ is non-collocated. To strictly enforce continuity between adjacent segments, we explicitly define an additional node at $\zeta_0^{(k)} = -1$. While this increases the number of variables, it decouples the interval boundaries and significantly simplifies the enforcement of continuity constraints, preventing the dependency chain typical of other formulations. The state at this node is retrieved through polynomial interpolation within each interval.

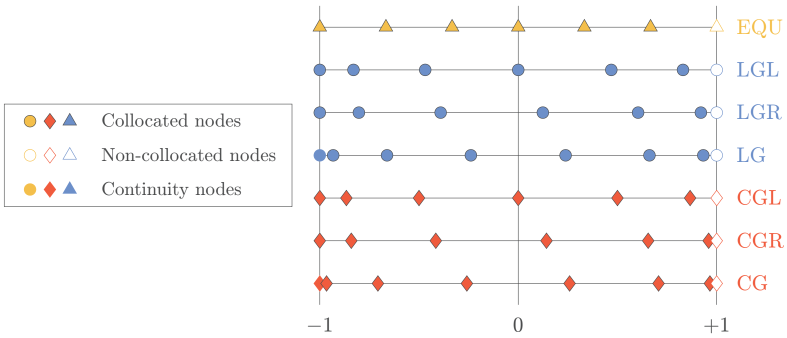

Figure 5. Families of pseudospectral collocation nodes.

Within each interval k, the derivative of the state approximation is obtained by analytically differentiating the polynomial vector $\mathbf{P}_{\mathbf{x}}^{(k)}(\zeta)$ with respect to the local variable ζ.[22] The derivative, $\dot{\mathbf{P}}_{\mathbf{x}}^{(k)}(\zeta)$, is evaluated at the collocation nodes $\zeta_m^{(k)}$ ($m = 1, \ldots, N_k$) using the pseudospectral differentiation matrix $D^{(k)}$ of size $N_k \times (N_k + 1)$. The elements of this matrix are constructed by evaluating the derivatives of the Lagrange basis polynomials at the collocation nodes:[52,53]

$$D_{m,n}^{(k)} = \left.\frac{\mathrm{d}\ell_n^{(k)}(\zeta)}{\mathrm{d}\zeta}\right|_{\zeta_m^{(k)}}, \quad (m = 1, \ldots, N_k,\ n = 1, \ldots, N_k + 1). \tag{18}$$

This matrix linearly maps the discrete state values to their corresponding temporal derivatives at the collocation points.[22,52] Note that $D^{(k)}$ depends solely on the node distribution and can be precomputed during initialization. The continuous-time differential equations in Eq. (8) are then transcribed into a set of algebraic constraints by equating the approximated derivative to the evaluated vector field at each collocation node.

Let $\tau_{k,m} = \tau(\zeta_m^{(k)})$ denote the discrete mesh points in the stroboscopic time domain. The continuous dynamics are collocated by enforcing

$$\sum_{n=1}^{N_k+1} D_{m,n}^{(k)}\, \mathbf{x}_n^{(k)} - \beta_k\, T_s\, \boldsymbol{f}\left(\mathbf{x}_m^{(k)}, \tau_{k,m}, \boldsymbol{\lambda}\right) = \mathbf{0}, \quad (m = 1, \ldots, N_k,\ k = 1, \ldots, K), \tag{19}$$

where β_k is the scaling factor arising from the chain rule between τ and ζ.

To ensure trajectory continuity at the interfaces between adjacent intervals, we require:

$$\mathbf{x}^{(k)}(+1) = \mathbf{x}^{(k+1)}(-1), \quad (k = 1, \ldots, K - 1). \tag{20}$$

The terminal state $\mathbf{x}^{(k)}(+1)$ coincides with the discrete state at the last node, $\mathbf{x}^{(k)}_{N_k+1}$. For Radau, Lobatto, and equidistant families, the initial state $\mathbf{x}^{(k+1)}(-1)$ coincides with the first node $\mathbf{x}^{(k+1)}_1$. For Gauss families, however, it corresponds to the explicitly added continuity node $\mathbf{x}^{(k+1)}_0$, whose value is obtained via polynomial interpolation:

$$\sum_{n=1}^{N_k+1} \ell^{(k)}_n(-1)\mathbf{x}^{(k)}_n - \mathbf{x}^{(k)}_0 = \mathbf{0}, \quad (k = 1, \ldots, K). \tag{21}$$

By sharing the numerical variable at the boundary, i.e., $\mathbf{x}^{(k)}_{N_k+1} \equiv \mathbf{x}^{(k+1)}_1$ (or $\mathbf{x}^{(k+1)}_0$ for Gauss methods), we implicitly satisfy continuity and avoid redundant constraints. The total number of 6-dimensional states for a quasi-periodic trajectory is $\mathcal{N}_K = 1 + \sum_{k=1}^{K} N_k$ for standard families, or $\mathcal{N}_K = 1 + \sum_{k=1}^{K}(N_k + 1)$ when the extra continuity node is required.

Computation of Invariant Tori

The computation of the invariant torus relies on two coupled discretization layers: a piecewise continuous polynomial approximation along the stroboscopic time, and a discrete Fourier representation across the set of reduced angles $\boldsymbol{\vartheta}$. The "skeleton" of the manifold is thus formed by a multidimensional grid of states $\mathbf{x}^{(k)}_{n,\boldsymbol{i}} \in \mathbb{R}^6$, where $k \in \{1, \ldots, K\}$ denotes the collocation interval, $n \in \{0, \ldots, N_k + 1\}$ identifies the discrete node, and $\boldsymbol{i} \in \mathcal{I}_{D-1}$ represents the reduced angle index on the invariant section. The total number of 6-dimensional states defining this skeleton is $\mathcal{N} = \mathcal{N}_F \mathcal{N}_K$.

To represent the dynamics of the entire invariant section simultaneously, we define the collected state vector $\mathbf{X}^{(k)}_n \in \mathbb{R}^{6\mathcal{N}_F}$ by stacking the individual states $\mathbf{x}^{(k)}_{n,\boldsymbol{i}}$ for all $\boldsymbol{i} \in \mathcal{I}_{D-1}$. Similarly, the collected vector field $\mathbf{F}(\mathbf{X}^{(k)}_n, \tau_{k,n}, \boldsymbol{\lambda}) \in \mathbb{R}^{6\mathcal{N}_F}$ is assembled by stacking the respective evaluations of $\boldsymbol{f}(\mathbf{x}^{(k)}_{n,\boldsymbol{i}}, \tau_{k,n}, \boldsymbol{\lambda})$. This vectorized formulation naturally casts the problem into a large-scale system of algebraic equations.

The unknowns in the numerical scheme comprise the global state vector $\mathbf{X} \in \mathbb{R}^{6\mathcal{N}}$, the unfolding parameters $\boldsymbol{\lambda} \in \mathbb{R}^{D_i}$, and a subset of the internal frequencies $\boldsymbol{\omega}$ (the exact number depends on the continuation setting, as one frequency is typically held fixed). External frequencies are assumed to be known a priori, being intrinsically determined by the dynamical model. In practice, the total number of unknowns, $6\mathcal{N} + D_i + D^{\omega}_i$ (where D^{ω}_i is the number of free internal frequencies), can reach several hundred thousand. At this scale, finite-difference approximations of the Newton Jacobian are computationally prohibitive, necessitating an analytical formulation; for brevity, the explicit expression of the Jacobian is omitted. The system is closed by imposing the following set of constraints.

Collocation Constraint For each angle $\boldsymbol{\vartheta}_{\boldsymbol{i}}$ characterizing the invariant section, the system dynamics are collocated at every node across all intervals. Consequently, the $\mathcal{N}_F$ stroboscopic trajectories $\mathbf{x}^{(k)}_{\boldsymbol{i}}(\zeta)$ are approximated by their respective polynomials $\mathbf{P}^{(k)}_{\mathbf{x}_{\boldsymbol{i}}}(\zeta)$, requiring the collocation constraint in Eq. (19) to be satisfied for every trajectory spanning the manifold.

Quasi-Periodicity Constraint The stroboscopic invariance condition in Eq. (7) is enforced at the first node of the first interval (τ_0) and the last node of the last interval (τ_K). The rigid rotation by $\boldsymbol{\rho} \in \mathbb{R}^{(D-1)}$ is applied via the rotation matrix $R : \mathbb{R}^{(D-1)} \to \mathbb{R}^{6\mathcal{N}_F \times 6\mathcal{N}_F}$. This operator performs a discrete Fourier transform to obtain the coefficients, applies a rigid rotation in the multi-frequency space by the input angle vector, and executes an inverse discrete Fourier transform to recover the states (see Reference 26). The discrete invariance condition is then formulated as:

$$\mathbf{X}^{(1)}_1 - R(-\boldsymbol{\rho})\mathbf{X}^{(K)}_{N_K+1} = \mathbf{0}. \tag{22}$$

This operation effectively counter-rotates the torus angle to compensate for the displacement induced by the stroboscopic flow.

Phase Constraint Because an invariant stroboscopic torus is a continuous manifold, any rigid rotation along its internal angles yields another valid parameterization of the same object.[18] This rotational invariance implies that the discrete stroboscopic section lacks a unique solution, which would lead to a rank-deficient

Jacobian matrix during differential correction. To isolate a unique parameterization and locally fix the internal phase, an additional set of phase constraints is enforced.

A robust approach is to impose an integral orthogonality condition between the current discrete section, represented by the stacked initial nodes $\widetilde{\mathbf{X}}_1^{(1)}$, and a known reference section $\widetilde{\mathbf{X}}_{1,\text{ref}}^{(1)}$ (typically the converged solution from the previous continuation step). For each internal angle θ_{d_i}, the phase constraint is:

$$\left(\frac{\partial \widetilde{\mathbf{X}}_{1,\text{ref}}^{(1)}}{\partial \theta_{d_i}}\right)^{\top} \left(\widetilde{\mathbf{X}}_1^{(1)} - \widetilde{\mathbf{X}}_{1,\text{ref}}^{(1)}\right) = 0, \quad (d_i = 1, \ldots, D_i). \tag{23}$$

The partial derivative of the reference state with respect to an internal angle can be evaluated using a matrix version of Eq. (15) (see Reference 45). When the stroboscopic angle is an internal angle (i.e., $s < D_i$), the derivative is retrieved from the infinitesimal invariance equation (5), evaluated at $\tau = 0$ with $\boldsymbol{\lambda} = \mathbf{0}$:

$$\frac{\partial \widetilde{\mathbf{X}}_1^{(1)}}{\partial \theta_s} = \frac{1}{\omega_s}\left(T_s\, \mathbf{F}(\mathbf{X}_1^{(1)}, 0, \mathbf{0}) - \frac{\partial \widetilde{\mathbf{X}}_1^{(1)}}{\partial \boldsymbol{\vartheta}}\boldsymbol{\omega}\right). \tag{24}$$

Error Control and Adaptive Layers

A consequence of the large-scale formulation is the requirement for rigorous handling of both trajectory propagation and torus parameterization. During continuation, invariant tori may undergo significant geometric distortions, which can degrade the quality of both the collocation discretization along the trajectories and the spectral representation along the angular directions. To maintain adequate resolution for the convergence and stability of the numerical scheme, while avoiding unnecessary growth in the number of decision variables, two adaptive correction layers are introduced.

Adaptive Collocation To efficiently achieve the desired accuracy, an adaptive mesh refinement algorithm is employed.[22] The mesh is iteratively updated based on a local error estimate. Unlike existing approaches that rely on explicit numerical integration (e.g., forward and backward time-marching),[22] the error in this framework is evaluated algebraically. Specifically, within each interval k, the state polynomials are interpolated at the midpoints between the existing grid nodes:

$$\zeta_{m+\frac{1}{2}}^{(k)} = \frac{1}{2}\left(\zeta_m^{(k)} + \zeta_{m+1}^{(k)}\right), \quad (m = 1, \ldots, N_k). \tag{25}$$

The interval error ε_k is defined as the maximum residual of the governing dynamics collocated at these midpoints, avoiding the need for secondary explicit simulations:

$$\varepsilon_k = \max_{\substack{1 \le m \le N_k \\ \boldsymbol{i} \in \mathcal{I}_{D-1}}} \left\| \dot{\mathbf{P}}_{\mathbf{x}_{\boldsymbol{i}}}^{(k)}(\zeta_{m+\frac{1}{2}}^{(k)}) - \beta_k\, T_s\, \widetilde{\mathbf{f}}\left(\mathbf{P}_{\mathbf{x}_{\boldsymbol{i}}}^{(k)}(\zeta_{m+\frac{1}{2}}^{(k)}), \tau(\zeta_{m+\frac{1}{2}}^{(k)})\right)\right\|_\infty. \tag{26}$$

Figure 6 illustrates the computation of the error estimate for a single state component.

Based on this midpoint error metric, the scheme dynamically adjusts the mesh resolution following the decision logic illustrated in Figure 7. This logic relies on a set of user-defined parameters and tolerances (e.g., $N_{\min}$, $N_{\max}$, $H_{\max}$, $\text{tol}_{\text{C,ref}}$, $\text{tol}_{\text{C,red}}$, and $\text{tol}_{C,\text{ext}}$) to trigger either a refinement or a reduction phase:

- **Mesh Refinement** (p-then-h): In regions where the local error exceeds the refinement tolerance ($\varepsilon_k \geq \text{tol}_{\text{C,ref}}$), the algorithm first attempts p-refinement by increasing the polynomial degree N_k. If this degree exceeds the upper bound $N_{\max}$, h-refinement is triggered, subdividing the mesh interval into H_k uniformly spaced intervals.
- **Mesh Reduction** (h-then-p): Conversely, in regions where the solution is sufficiently smooth and the error falls below the reduction tolerance ($\varepsilon_k < \text{tol}_{\text{C,red}}$), the algorithm attempts to coarsen the mesh. It first evaluates the feasibility of h-reduction by extrapolating the solution to the adjacent interval. If the maximum extrapolation error Δ_k remains below $\text{tol}_{\text{C,ext}}$, the intervals are merged. If this criterion is not met, the algorithm defaults to p-reduction, decreasing the polynomial degree.

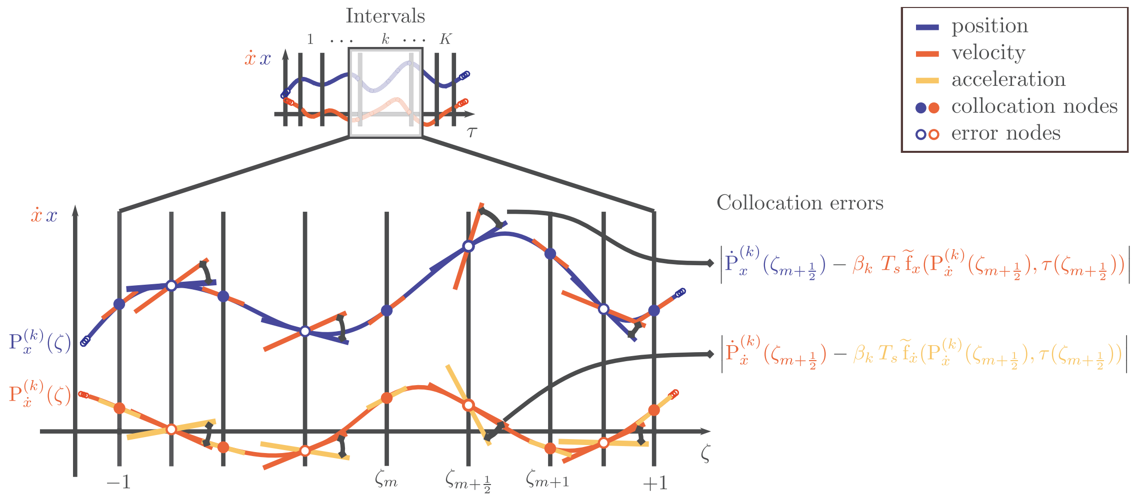

Figure 6. Illustration of the collocation error estimator used for adaptive collocation.

This combined hp-refinement and hp-reduction process guarantees that the required resolution is maintained for sensitive trajectory arcs, while unnecessary decision variables are systematically eliminated without compromising the validity of the trajectory.

Adaptive Spectral Resolution Given that invariant surfaces are analytic, their Fourier series coefficients exhibit exponential decay. This property is exploited to optimize the angular parameterization by continuously monitoring the amplitudes of the discrete Fourier coefficients $\mathbf{c}_{\boldsymbol{j}}$ on a representative set of stroboscopic sections. To maintain granular control over the resolution, the spectral content of each of the $D-1$ angular dimensions is assessed independently. For each dimension $d \in \{1, \ldots, D-1\}$, an adaptive strategy dynamically adjusts the maximum frequency index M_{F_d} based on two user-defined spectral tolerances, $\mathrm{tol}_{\mathrm{F,ref}}$ and $\mathrm{tol}_{\mathrm{F,red}}$:

- **Spectral Refinement:** If the maximum coefficient magnitude at the highest frequency index ($|j_d| = M_{F_d}$) exceeds $\mathrm{tol}_{\mathrm{F,ref}}$ for any coordinate and any evaluated section, M_{F_d} is incremented by 1 to enhance spectral resolution.

- **Spectral Reduction:** Conversely, if the maximum magnitude of the coefficients at the two highest frequencies ($|j_d| \in \{M_{F_d} - 1, M_{F_d}\}$) falls strictly below $\mathrm{tol}_{\mathrm{F,red}}$ across all sections and coordinates, the spectral bound M_{F_d} is decremented by 1 to remove redundant degrees of freedom.

Whenever a modification to the polynomial degree or the Fourier order is triggered, the computed solution is projected onto the updated discretization grid. This is achieved via Lagrange interpolation in the temporal domain, combined with a re-evaluation of the coefficients through the discrete Fourier transform on the new angular grid.

Pseudo-Arclength Continuation

To compute families of invariant tori, a pseudo-arclength continuation (PAC) scheme is employed.[54] The algorithm relies on a predictor step to estimate the next solution along the family branch, followed by a corrector step to ensure the new solution satisfies the governing equations.

Let $\mathbf{Y} = [\mathbf{X}^\top, \boldsymbol{\lambda}^\top, p]^\top$ denote the global vector of unknowns, where p represents the continuation parameter. Given a previously converged solution $\overline{\mathbf{Y}}$, the local direction of the family is approximated by a tangent vector $\delta\overline{\mathbf{Y}}$, typically derived via a secant predictor from two previously computed solutions.

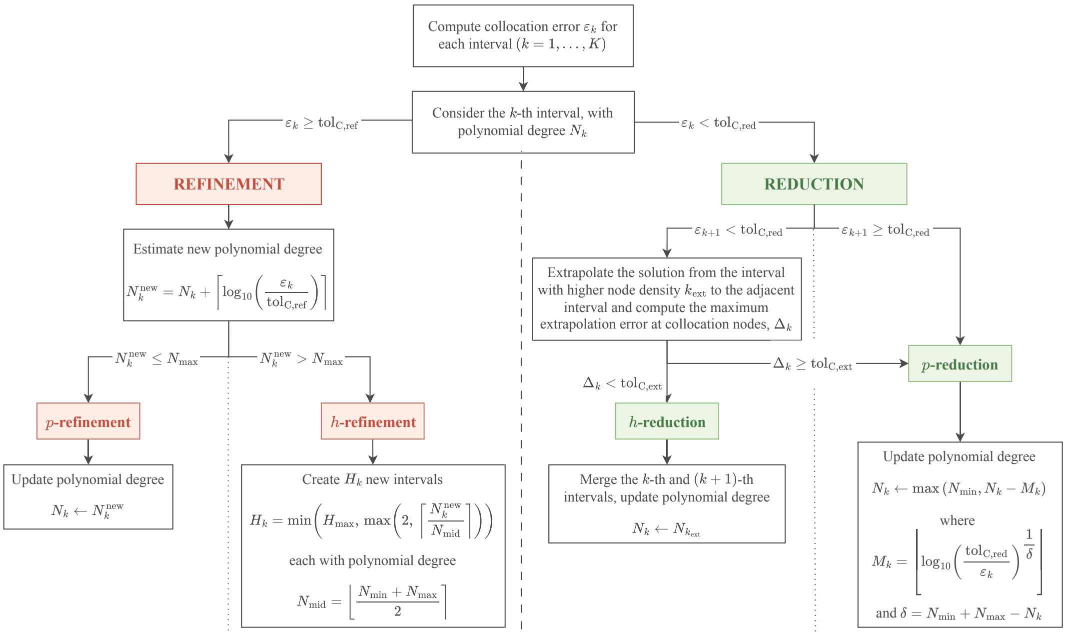

Figure 7. Schematic representation of the adaptive mesh refinement and reduction logic.

The PAC introduces a scalar constraint that forces the new solution $\mathbf{Y}$ to lie on a hyperplane orthogonal to $\delta\overline{\mathbf{Y}}$, at a prescribed pseudo-arclength distance $\Delta\varsigma$ from $\overline{\mathbf{Y}}$. Since the discretized state vector $\mathbf{X} \in \mathbb{R}^{6\mathcal{N}}$ contains significantly more elements than the remaining parameters $(\boldsymbol{\lambda}, p)$, a standard Euclidean dot product would be overwhelmingly dominated by the spatial components. To prevent this numerical imbalance, we define a weighted inner product $\langle\cdot,\cdot\rangle_W$. Let $\mathbf{v}$ and $\mathbf{w}$ be two augmented vectors partitioned as $\mathbf{v} = [\mathbf{v}_X^\top, \mathbf{v}_q^\top]^\top$, where $\mathbf{v}_X$ represents the discretized states and $\mathbf{v}_q$ encompasses the remaining scalar parameters. The weighted inner product is defined as:[23]

$$\langle\mathbf{v},\mathbf{w}\rangle_W = \frac{1}{6\mathcal{N}}(\mathbf{v}_X^\top \mathbf{w}_X) + (\mathbf{v}_q^\top \mathbf{w}_q). \tag{27}$$

The tangent vector is strictly normalized with respect to this metric, such that $\|\delta\overline{\mathbf{Y}}\|_W^2 = \langle\delta\overline{\mathbf{Y}}, \delta\overline{\mathbf{Y}}\rangle_W = 1$. The pseudo-arclength constraint is then:

$$\langle\delta\overline{\mathbf{Y}}, (\mathbf{Y} - \overline{\mathbf{Y}})\rangle_W = \Delta\varsigma, \tag{28}$$

and the predictor step is

$$\mathbf{Y} = \overline{\mathbf{Y}} + \Delta\varsigma\,\delta\overline{\mathbf{Y}}. \tag{29}$$

The continuation is applied across three distinct cases, each with a specific continuation parameter p:

Internal Continuation This phase is utilized to compute the QHVO family within the CR3BP by expanding a known HVO into a 2D invariant torus. The stroboscopic time $T_s = 2\pi m_{\mathrm{SEM}}\,\mathrm{TU}_{\mathcal{H}}$ is kept fixed, while the continuation is driven by varying the reduced internal frequency ($p = \omega_1$).

External Continuation: CR3BP to HR4BP This transition lifts the dynamics from the CR3BP to the HR4BP,[24] converting a PO into a 2D invariant torus. In this case, the continuation parameter is the mass parameter of the HR4BP ($p = m$), which is gradually increased from 0 to its physical value m_{SEM}.

External Continuation: HR4BP to IQHR4BP The final continuation elevates the 2D invariant torus obtained in the HR4BP into a 3D invariant torus within the IQHR4BP. For this dynamical transition, the varying parameter is the lunar orbital eccentricity ($p = e_{\mathrm{M}}$), which is increased from 0 to its true physical value e_{M}.

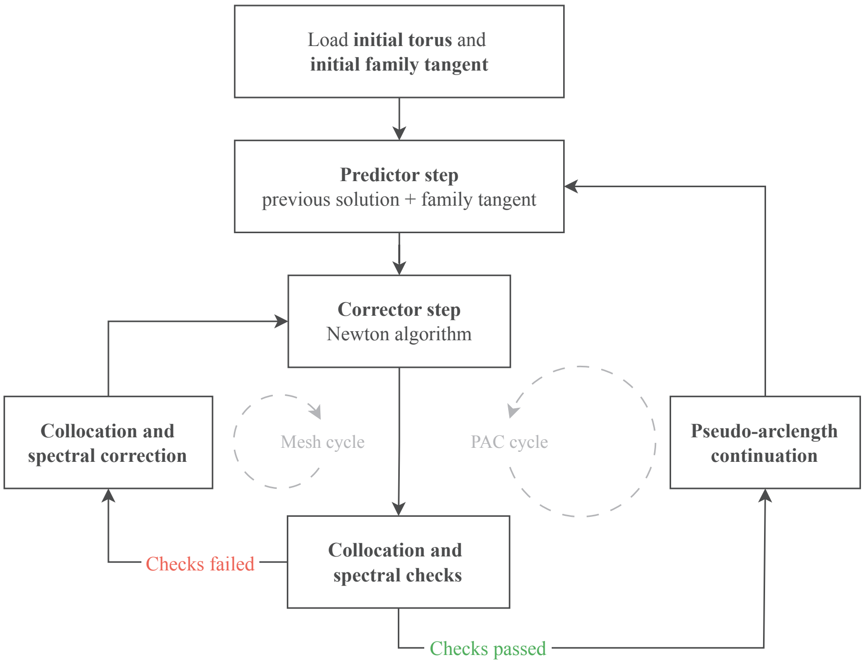

Figure 8. Flowchart illustrating the nested algorithmic cycles for the continuation of invariant tori.

Solving the System of Equations

Once an initial guess is provided by the predictor, the corrector step aims to determine the exact roots of the large-scale nonlinear system $\mathbf{H}(\mathbf{Y}) = \mathbf{0}$. The system is square, with the total number of unknowns, $6\mathcal{N} + D_i + 1$, matching the number of scalar equations (comprising $6\mathcal{N} - 6\mathcal{N}_F$ collocation constraints, $6\mathcal{N}_F$ quasi-periodic boundary conditions, D_i phase constraints, and 1 pseudo-arclength constraint).

To find the roots, a multidimensional Newton-Raphson scheme is employed. Given an initial guess $\mathbf{Y}^{(0)}$, the solution is updated at each iteration j as:

$$\mathbf{Y}^{(j+1)} = \mathbf{Y}^{(j)} + \Delta\mathbf{Y}^{(j)}. \tag{30}$$

The correction vector $\Delta\mathbf{Y}^{(j)}$ is computed by solving the linear system:

$$\mathbf{JH}(\mathbf{Y}^{(j)})\Delta\mathbf{Y}^{(j)} = -\mathbf{H}(\mathbf{Y}^{(j)}), \tag{31}$$

where $\mathbf{JH}(\mathbf{Y}) = \partial\mathbf{H}/\partial\mathbf{Y}$ is the square Jacobian matrix. As previously noted, evaluating this matrix via finite differences is computationally prohibitive; thus, $\mathbf{JH}(\mathbf{Y})$ is derived and assembled analytically. Despite its large dimension, the Jacobian matrix is highly sparse and block-banded, allowing for efficient computation via sparse direct linear solvers.

The iterative process continues until the maximum absolute residual falls below the prescribed tolerance $\|\mathbf{H}(\mathbf{Y}^{(j)})\|_\infty < \text{tol}_{\text{N,res}}$, or the correction step magnitude satisfies $\|\Delta\mathbf{Y}^{(j)}\|_\infty < \text{tol}_{\text{N,step}}$. If the residual exceeds the divergence threshold $\|\mathbf{H}(\mathbf{Y}^{(j)})\|_\infty > \text{tol}_{\text{N,max}}$, the Newton-Raphson scheme is immediately aborted. In this event, discretization error checks are bypassed; the current step is discarded, and the algorithm automatically halves the pseudo-arclength step $\Delta\varsigma$ to retry the continuation from the last converged solution.

Upon successful Newton convergence, the solution quality is assessed against the collocation and Fourier error tolerances. If the checks are satisfied, the solution is accepted, and the algorithm proceeds to the next

PAC step. Conversely, if either tolerance is violated or the maximum number of Newton iterations $N_{\text{iter,max}}$ is reached, a mesh iteration cycle is triggered. In this scenario, the pseudo-arclength step $\Delta\varsigma$ is kept constant, and the most recent solution is resampled onto the adapted mesh to serve as the new initial guess. The nested cycle logic is outlined in Figure 8.

To prevent computational stalling, a maximum number of consecutive mesh iterations is enforced. If a satisfactory discretization is not achieved within this limit, the algorithm reverts to the previous solution and halves $\Delta\varsigma$. Furthermore, to manage the dimensionality of the discretized state, a hard upper bound $n_{\text{var,max}}$ is imposed; if a triggered mesh iteration requires variables exceeding this limit, the adaptation is aborted, and $\Delta\varsigma$ is halved instead.

To optimize the continuation process, a heuristic automatically adjusts the pseudo-arclength step size based on the convergence performance of the Newton-Raphson scheme.[54] This adaptive policy compares the number of iterations required to achieve convergence, N_{iter}, relative to a target value, N_{opt}: the step size is doubled if $N_{\text{iter}} < 2N_{\text{opt}}$, and halved if $N_{\text{iter}} \geq 2N_{\text{opt}}$.

Operational bounds are strictly enforced on $\Delta\varsigma$: if the adaptation logic suggests a step exceeding $\Delta\varsigma_{\text{max}}$, it is capped accordingly; conversely, if the step size drops below $\Delta\varsigma_{\text{min}}$, the continuation is formally terminated to avoid numerical stagnation. Finally, a dedicated safeguard evaluates the unfolding parameters $\boldsymbol{\lambda}$ upon convergence. If their norm exceeds tol_{ufp} without triggering a standard mesh iteration, a Fourier refinement is forced across all angular dimensions. This intervention is necessary because, on an insufficiently resolved grid, the nonlinear solver may artificially inflate the unfolding parameters to satisfy the constraints.

Table 1. Numerical settings and parameters adopted.

Category	Parameter	Value (nondim.)	Description
Collocation	Node family	CG	Shared variables at interval boundaries
	N_{min}, N_{max}	$[6, 16]$	Allowed polynomial degree range
	H_{max}	3	Maximum h-refinement intervals
	$\text{tol}_{\text{C,ref}}$	10^{-11}	Refinement tolerance
	$\text{tol}_{\text{C,red}}$	10^{-12}	Reduction tolerance
	$\text{tol}_{\text{C,ext}}$	10^{-6}	Extrapolation tolerance
	$n_{\text{var,max}}$	7×10^5	Maximum number of variables
Fourier	$\text{tol}_{\text{F,ref}}$	10^{-9}	Refinement tolerance
	$\text{tol}_{\text{F,red}}$	10^{-11}	Reduction tolerance
Newton	$N_{\text{iter,max}}$	10	Maximum consecutive iterations
	N_{opt}	8	Target iterations
	$\text{tol}_{\text{N,res}}$	2.5×10^{-12}	Residual tolerance
	$\text{tol}_{\text{N,max}}$	10	Maximum admissible residual
	$\text{tol}_{\text{N,step}}$	10^{-13}	Step tolerance
	tol_{ufp}	10^{-12}	Unfolding parameter tolerance

RESULTS

This section demonstrates the application of the methodology, first to compute a family of QHVOs in the H3BP, and subsequently to transition POs from the CR3BP into 3D QPOs within the IQHR4BP. All numerical simulations were performed on a workstation running MATLAB R2025b on an Intel Core i7-10700 CPU @ 2.90 GHz (8 physical cores) with 16 GB of RAM. The numerical settings adopted throughout these simulations are summarized in Table 1.

Parallelization was leveraged to accelerate the assembly of the constraint vector and the Jacobian, which is stored and processed as a sparse matrix. Barycentric weights are used for interpolation to enhance numerical stability. Collocation differentiation matrices and barycentric weights are precomputed during initialization for each admissible polynomial degree ($N_{\text{min}} \leq N \leq N_{\text{max}}$). Similarly, the Fourier rotation operator R is precomputed offline and updated only when a change in the Fourier order is triggered.

Family of QHVO

The computation of the QHVO family is initiated by exciting the center manifold of a baseline HVO. Once the reference periodic orbit is established, an initial collocation mesh is constructed utilizing Chebyshev-Gauss (CG) nodes across $K = 10$ intervals (see Appendix C for details regarding the mesh generation strategy). To construct the initial invariant curve, the monodromy matrix is evaluated at a specific phase angle $\theta_1 = 0$ along the HVO, defined here as the orbit's rightmost intersection with the ζ-axis (black dot in Figure 9). From this matrix, a complex conjugate pair of eigenvalues, (ϕ_1, ϕ_2), with unitary magnitude is extracted; specifically, the pair whose associated eigenvectors lie primarily within the (ζ, η) plane. The new internal frequency is initialized as $\omega = \omega_2 = \rho/T_1$, where $\rho = 2\pi + \arg(\phi_1)$.[55] A preliminary approximation of the stroboscopic torus is then generated by exploiting the eigenvector $\mathbf{u}$ associated with the selected eigenvalue:[21,23,44,46]

$$\boldsymbol{\sigma}(\vartheta, 0) = \epsilon \left(\mathrm{Re}(\mathbf{u})\cos(\vartheta) - \mathrm{Im}(\mathbf{u})\sin(\vartheta)\right), \tag{32}$$

where ϵ represents a small, arbitrary excitation amplitude, here set to 10^{-4}. This initial stroboscopic curve is discretized using $N_{F_2} = 25$ evenly spaced angles. Finally, these discretized states $\mathbf{X}_0^{(1)}$ are propagated forward over one full stroboscopic period ($T_1 = 1/m_{\mathrm{SEM}}$). The states evaluated at the collocation nodes during this propagation are stored to assemble the skeleton of the torus $\mathbf{X}$, which, alongside two unfolding parameters $\boldsymbol{\lambda}$ and the second internal frequency ω, serves as the initial predictor for the continuation family. The total number of unknowns is 24 603.

For each computed 2D torus, the equivalent eccentricity of the lunar orbit is estimated following the methodology provided in Reference 9. The continuation process is executed over 300 PAC iterations using a constant pseudo-arclength step $\Delta\varsigma = 5 \times 10^{-4}$. Both the step size and the Fourier order are intentionally kept fixed to generate a dense and homogeneously populated solution branch, which facilitates subsequent interpolation procedures. The computation of this entire branch requires 3 minutes and 55 seconds, reaching a final equivalent eccentricity of $e \approx 0.0648$. Some stroboscopic trajectories departing from the invariant section of the SEM QHVO are shown in Figure 9.

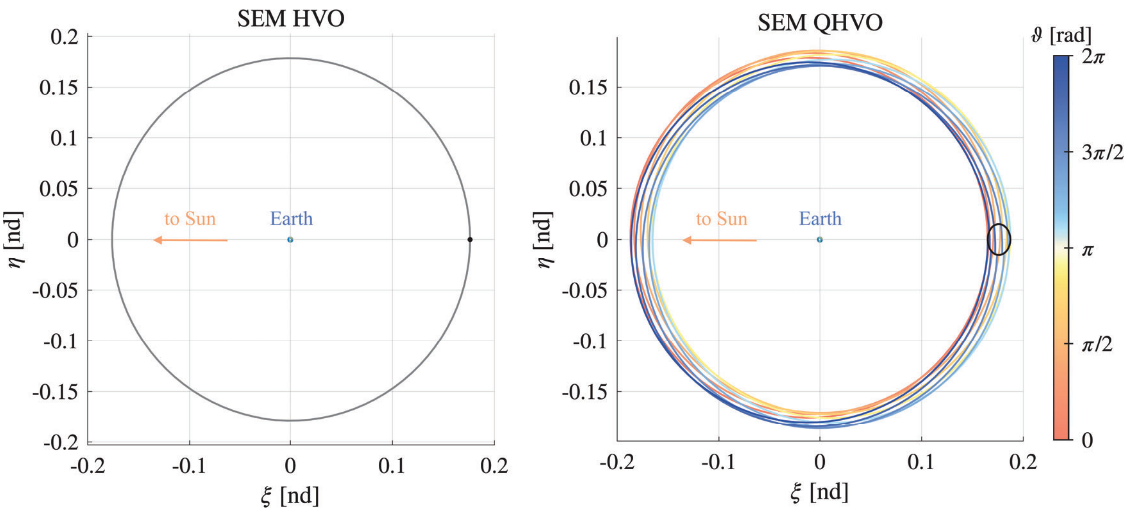

Figure 9. The HVO and QHVO in the $\mathcal{H}$ frame. The stroboscopic point and curve are depicted in black, while the trajectories are color-coded based on their initial phase angle along the stroboscopic section.

Each converged invariant torus is ultimately stored in terms of its Fourier coefficients, $\mathbf{c}_j$. However, the torus skeleton generated by the corrector scheme consists of N_{F_2} stroboscopic trajectories, evaluated at the non-uniform collocation mesh nodes $\tau_{k,n}$. To properly extract the coefficients $\mathbf{c}_j$ that approximate the torus function, these trajectories are first interpolated onto an evenly spaced grid in the normalized stroboscopic time τ, of size $N_{F_1} = 25$. Subsequently, the states along each invariant curve are rotated backward via a Fourier rotation by an amount equal to $\tau\rho$. This transformation reconstructs the state grid $\mathbf{x}_i$ at the uniform angular nodes $\boldsymbol{\theta}_i$, allowing for the direct application of Eq. (10). The magnitudes of the resulting Fourier coefficients are provided in Figure 10. As shown, the coefficients corresponding to even indices along θ_1 are strictly null. This half-wave symmetry is an intrinsic property inherited directly from the underlying symmetries of the H3BP. This characteristic is actively exploited by storing only the odd-indexed coefficients, which effectively halves the memory footprint and accelerates the subsequent evaluations of the dynamics within the IQHR4BP. Notably, these internal algebraic symmetries are also consistent with the HR4BP, whose fundamental period corresponds exactly to half a synodic month.

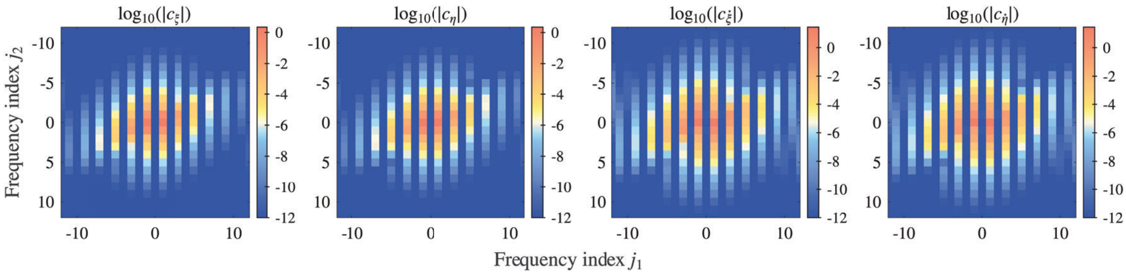

Figure 10. Magnitude of the Fourier coefficients of the QHVO across the different state coordinates.

From Periodic Orbits to 3D Invariant Tori

Periodic orbits of the CR3BP are first transitioned into the HR4BP, where they evolve into two-dimensional invariant tori, before ultimately being continued into the IQHR4BP.

The first external continuation phase is executed by incorporating the HR4BP mass parameter m into the vector of unknowns, alongside one unfolding parameter. For each iterative value of m, the corresponding member of the variational orbit family is determined using the Fourier series representation detailed in Appendix B. The stroboscopic period is selected to match the internal period of the CR3BP orbit. This choice is motivated by the observation that fewer Fourier coefficients are required to accurately resolve the invariant curve associated with the external phase.[17] Note that, because the characteristic reference units depend strictly on m, they evolve continuously during the continuation process. Consequently, the nondimensional stroboscopic time must be dynamically rescaled at each step, whereas the external frequency ω_e remains constant at $2\ \mathrm{rad}/\mathrm{TU}_\mathcal{S}$.

To initialize the algorithm, a preliminary predictor is generated by stacking $N_{F_1} = 11$ identical copies of the original periodic orbit's discretized states. During the subsequent collocation scheme, the extended flow defined in Eq. (2) is evaluated at each discrete state of the stroboscopic curve using a different external angle $\vartheta = \theta_{e_1}$. This effectively simulates a set of distinct initial phases along the underlying HVO. The PAC framework employs the adaptive refinement logic for both the temporal mesh and the Fourier discretization, terminating automatically once the physical mass parameter m_{SEM} is reached. This robust transition from the CR3BP to the HR4BP typically requires 5 to 8 PAC steps, converging within seconds of computational time.

The final step consists of the external continuation into the IQHR4BP by varying the equivalent eccentricity of the underlying QHVO. To achieve this, the PAC scheme is augmented by including the lunar eccentricity parameter e_M in the vector of unknowns. For each iterative value of e_M, the corresponding QHVO baseline is retrieved by interpolating the dense set of 300 solutions previously computed during the internal continuation phase. The two external frequencies governing the quasi-periodic perturbation are concurrently updated: the synodic frequency ω_{e_1} remains fixed at $2\ \mathrm{rad}/\mathrm{TU}_\mathcal{S}$, whereas the anomalistic frequency ω_{e_2} naturally evolves as a function of the eccentricity.

Analogously to the previous transition, the initial predictor is constructed by stacking $N_{F_2} = 11$ identical copies of the converged two-dimensional invariant torus. During the collocation procedure, the quasi-periodic

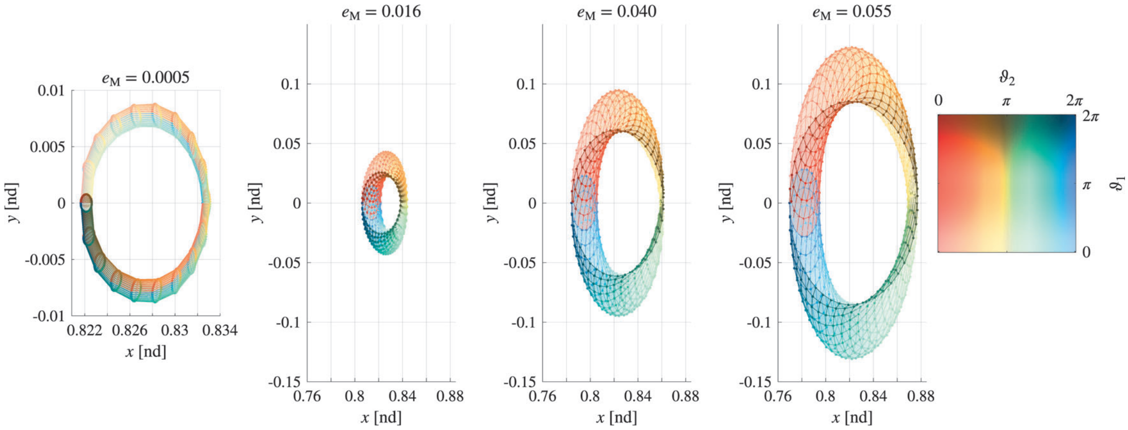

Figure 11. Evolution of the stroboscopic invariant section of a Halo-L_1 orbit during the continuation from the HR4BP to the IQHR4BP, in the $\mathcal{S}$ frame.

vector field defined in Eq. (3) is evaluated across the two-dimensional angle grid $\boldsymbol{\vartheta} = \boldsymbol{\theta}_e$, simulating the complete set of initial phases characterizing the quasi-periodic system. At this stage, the problem dimensionality increases, resulting in a high-dimensional system with hundreds of thousands of variables. Consequently, the exact inversion of the large-scale Jacobian matrix within the Newton-Raphson scheme dominates the computational effort.

Overall, the PAC branch transitioning from the HR4BP to the IQHR4BP typically requires minutes. The most critical parameter governing this cost is the Fourier refinement tolerance, $\mathrm{tol}_{\mathrm{F,red}}$. For comparison, transitioning a specific Halo orbit requires approximately 3 minutes using $\mathrm{tol}_{\mathrm{F,red}} = 10^{-6}$ (resulting in $120\,044$ variables), whereas the computational time increases to 6 minutes when tightening the tolerance to $\mathrm{tol}_{\mathrm{F,red}} = 10^{-8}$ (yielding $192\,986$ variables). Figure 11 illustrates the evolution of the stroboscopic invariant section of a Halo-L_1 orbit during the external continuation from the HR4BP to the IQHR4BP. The progressive deformation of the surface highlights the effect of the increasing lunar eccentricity.

Once the invariant torus has been successfully transitioned into the IQHR4BP, it is stored in the form of a torus function parameterized by its Fourier coefficients, analogously to the representation adopted for the QHVO solutions. The resulting Fourier representation is then used to validate the invariance of the computed manifold: some trajectory initialized on the torus are propagated using the full dynamical model and compared against the corresponding torus function evolution, verifying the consistency between the numerical propagation and the quasi-periodic parameterization.

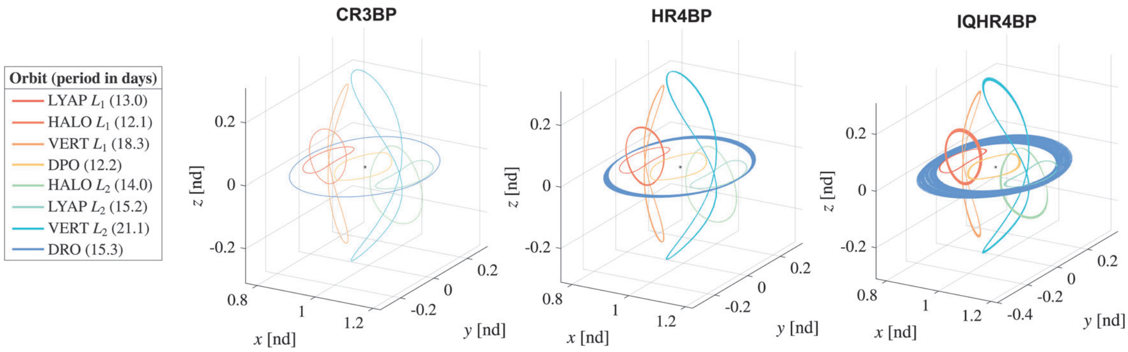

Figure 12. Sample POs transitioned from the CR3BP to the IQHR4BP. All trajectories are represented in the $\mathcal{P}$ frame.

Figure 12 illustrates a selection of periodic orbits transitioned across the models. For orbits in close proximity to the Moon, the geometric thickness of the resulting two-dimensional tori in the HR4BP remains relatively small, as solar perturbation acts as a second-order effect in this region.[3] Conversely, larger orbits, such as the distant retrogade orbit (DRO), exhibit a significantly wider spatial spread. Upon transitioning to the IQHR4BP, the resulting three-dimensional invariant tori become noticeably thicker across all families. This geometric expansion is particularly pronounced for the DRO; as primarily an in-plane orbit, it is highly sensitive to the introduction of the Earth–Moon orbital eccentricity, which strongly amplifies the in-plane dynamics.

Visualizing the three-dimensional invariant tori within the $\mathcal{S}$ frame provides a more intuitive representation of the quasi-periodic motion. Figure 13 illustrates this concept for two 3D QPOs alongside a close-up view of their invariant surfaces $\Sigma^{(1,0)}$. To further characterize the high-dimensional topology of these manifolds, a detailed breakdown of the invariant surfaces is provided in Appendix D.

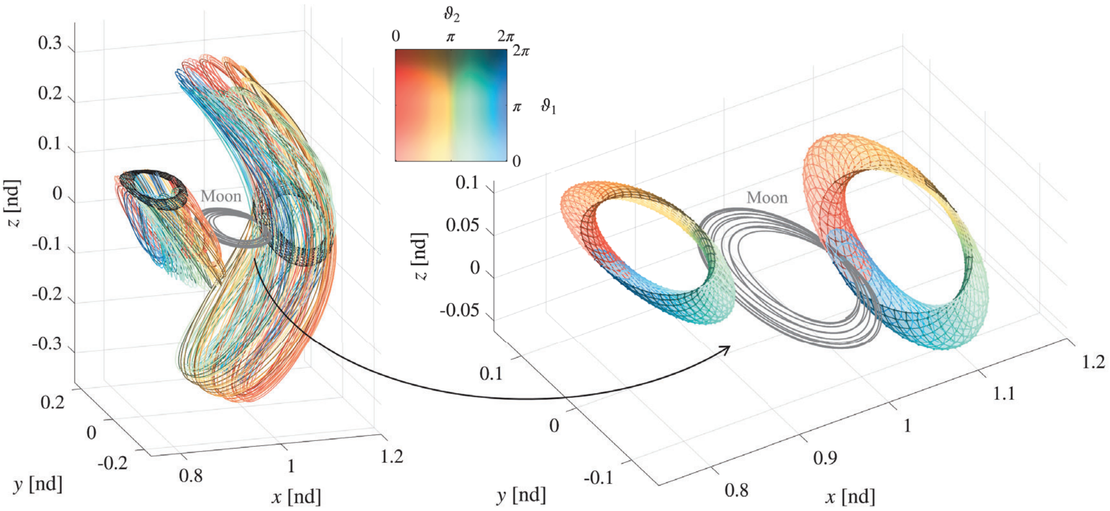

Figure 13. QPOs of the L_1-Halo and L_2-Vertical families in the IQHR4BP, shown in the $\mathcal{S}$ frame. The left panel displays the stroboscopic trajectories generated from the invariant sections $\sigma^{(1)}(\vartheta, 0)$ (in black). The right panel provides a zoomed-in view of the two invariant sections. The color coding corresponds to the reduced angles ϑ.

CONCLUSIONS

This work establishes a robust numerical framework for the systematic computation of three-dimensional invariant tori within the IQHR4BP. By introducing a dual-layer adaptive strategy that dynamically couples an adaptive collocation scheme for time propagation with a spectral resolution adjustment for the angular parameterization, the severe numerical sensitivities and dimensionality bottlenecks typical of high-order tori are effectively mitigated. Through this approach, fundamental families of periodic orbits from the CR3BP were successfully transitioned into three-dimensional quasi-periodic trajectories within the Earth–Moon system.

The results demonstrate that this hierarchical continuation strategy efficiently bridges simplified dynamical models and high-fidelity formulations while preserving the underlying invariant structures. The computed tori also provide valuable insight into the influence of solar perturbations and lunar orbital eccentricity on the phase-space geometry. Overall, the proposed framework enables the systematic exploration of high-fidelity quasi-periodic dynamics and provides accurate initial guesses for trajectory design in full-ephemeris models

REFERENCES

[1] G. Gómez, J. J. Masdemont, and J. M. Mondelo, "Solar system models with a selected set of frequencies," *Astronomy & Astrophysics*, Vol. 390, July 2002, pp. 733–749, doi: 10.1051/0004-6361:20020625.

[2] D. A. Dei Tos and F. Topputo, "On the advantages of exploiting the hierarchical structure of astrodynamical models," *Acta Astronautica*, Vol. 136, jul 2017, pp. 236–247, doi: 10.1016/j.actaastro.2017.02.025.

[3] B. Park and K. C. Howell, "Assessment of dynamical models for transitioning from the Circular Restricted Three-Body Problem to an ephemeris model with applications," *Celestial Mechanics and Dynamical Astronomy*, Vol. 136, Feb. 2024, doi: 10.1007/s10569-023-10178-9.

[4] V. Szebehely and G. E. Giacaglia, "On the elliptic restricted problem of three bodies," *The Astronomical Journal*, Vol. 69, No. 3, 1964, pp. 230–235.

[5] S. Huang, "Very restricted four-body problem," *Publications of Goddard Space Flight Center*, Vol. 354, 1960.

[6] D. Villegas-Pinto, N. Baresi, S. Locoche, and D. Hestroffer, "Resonant quasi-periodic near-rectilinear Halo orbits in the Elliptic-Circular Earth-Moon-Sun Problem," *Advances in Space Research*, Vol. 71, Jan. 2023, pp. 336–354, doi: 10.1016/j.asr.2022.08.011.

[7] L. Mohn and J. Kevorkin, "Some limiting cases of the restricted four-body problem," *The Astronomical Journal*, Vol. 72, Oct. 1967, p. 959, doi: 10.1086/110370.

[8] D. J. Scheeres, "The Restricted Hill Four-Body Problem with Applications to the Earth–Moon–Sun System," *Celestial Mechanics and Dynamical Astronomy*, Vol. 70, No. 2, 1998, pp. 75–98, doi: 10.1023/a:1026498608950.

[9] B. Park, R. R. Sanaga, and K. C. Howell, "A frequency-based hierarchy of dynamical models in cislunar space: leveraging periodically and quasi-periodically perturbed models," *Celestial Mechanics and Dynamical Astronomy*, Vol. 137, Jan. 2025, doi: 10.1007/s10569-025-10236-4.

[10] B. Park, R. R. Sanaga, and K. C. Howell, "Bridging ephemeris transition gaps: Quasi-periodic extensions for the Hill Restricted Four-Body Problem in cislunar space," *Acta Astronautica*, Apr. 2025, doi: 10.1016/j.actaastro.2025.03.033.

[11] G. M. Brown and D. J. Scheeres, "Quasi-Periodic Orbits Around the 9:2 NRHO in the Inclined Elliptic Hill Restricted 4-Body Problem," *AAS/AIAA Astrodynamics Specialist Conference*, Boston, Massachusetts, US, Aug. 2025.

[12] G. M. Brown, D. B. Henry, and D. J. Scheeres, "Constructing High-Fidelity Spacecraft Trajectory Baselines with Higher-Dimensional Invariant Tori," *76th International Astronautical Congress*, No. IAC-25-C1.8.3(102931), Sydney, Australia, Sept. 2025.

[13] G. M. Brown and D. J. Scheeres, "Orbit Capacity of Higher-Dimensional Tori Around Gateway," *Journal of Guidance, Control, and Dynamics*, Vol. 49, Mar. 2026, pp. 879–893, doi: 10.2514/1.g009219.

[14] R. R. Sanaga, B. Park, and K. C. Howell, "Systematic Numerical Transitions of Cislunar Trajectories Across Dynamical Models," *The Journal of the Astronautical Sciences*, Vol. 73, Feb. 2026, doi: 10.1007/s40295-026-00571-5.

[15] Á. Jorba and J. Villanueva, "On the Persistence of Lower Dimensional Invariant Tori under Quasi-Periodic Perturbations," *Journal of Nonlinear Science*, Vol. 7, No. 5, 1997, pp. 427–473, doi: 10.1007/s003329900036.

[16] N. Baresi, Z. P. Olikara, and D. J. Scheeres, "Fully Numerical Methods for Continuing Families of Quasi-Periodic Invariant Tori in Astrodynamics," *The Journal of the Astronautical Sciences*, Vol. 65, Jan. 2018, pp. 157–182, doi: 10.1007/s40295-017-0124-6.

[17] D. B. Henry and D. J. Scheeres, "A Flow map Parameterization Method for Quasi-periodic Orbit Computation in the Hill Restricted Four-body Problem," *AAS/AIAA Astrodynamics Specialist Conference*, Broomfield, Colorado, USA, Aug. 2024.

[18] E. Castellà and Á. Jorba, "On the vertical families of two-dimensional tori near the triangular points of the Bicircular problem," *Celestial Mechanics and Dynamical Astronomy*, Vol. 76, No. 1, 2000, pp. 35–54, doi: 10.1023/a:1008321605028.

[19] G. Gómez and J. Mondelo, "The dynamics around the collinear equilibrium points of the RTBP," *Physica D: Nonlinear Phenomena*, Vol. 157, No. 4, 2001, pp. 283–321, doi: 10.1016/S0167-2789(01)00312-8.

[20] Z. P. Olikara and D. J. Scheeres, "Numerical method for computing quasi-periodic orbits and their stability in the restricted three-body problem," *Advances in the Astronautical Sciences*, Vol. 145, Mar. 2012, pp. 911–930.

[21] Z. P. Olikara, *Computation of Quasi-Periodic Tori and Heteroclinic Connections in Astrodynamics Using Collocation Techniques*. phdthesis, University of Colorado Boulder, 2016.

[22] G. V. Haman and A. V. Rao, "Adaptive Mesh Refinement and Error Estimation Method for Optimal Control Using Direct Collocation," *Journal of Dynamic Systems, Measurement, and Control*, Vol. 147, June 2025, doi: 10.1115/1.4068206.

[23] D. B. Henry, J. J. Rosales, G. M. Brown, and D. J. Scheeres, "Quasi-periodic orbits around Earth-Moon L1 and L2 in the Hill restricted four-body problem," *AIAA/AAS Astrodynamics Specialist Conference*, Big Sky, Montana, American Institute of Aeronautics and Astronautics, Aug. 2023.

[24] G. Grossi and F. Topputo, "Computation of Invariant Tori in the Hill Restricted 4-Body Problem via Collocation," *AAS/AAIA Space Flight Mechanics Meeting*, Kauai, Hawaii, USA, Jan. 2025.

[25] C. Aydin, "From Babylonian lunar observations to Floquet multipliers and Conley–Zehnder indices," *Journal of Mathematical Physics*, Vol. 64, Aug. 2023, doi: 10.1063/5.0156959.

[26] B. P. McCarthy and K. C. Howell, "Leveraging quasi-periodic orbits for trajectory design in cislunar space," *Astrodynamics*, Vol. 5, Jan. 2021, pp. 139–165, doi: 10.1007/s42064-020-0094-5.

[27] Y. Sun, M. Wang, and H. Zhang, "Distant retrograde orbit baseline generation considering solar eclipse mitigation," *Acta Astronautica*, Vol. 223, 2024, pp. 221–233, doi: 10.1016/j.actaastro.2024.06.038.

[28] D. B. Henry and D. J. Scheeres, "Expansion Maps: Designing Relative Trajectories on Quasi-Periodic Orbits," *Journal of Guidance, Control, and Dynamics*, Vol. 44, Mar. 2021, pp. 457–468, doi: 10.2514/1.g005492.

[29] N. Baresi, *Transition of Two-Dimensional Quasi-periodic Invariant Tori in the Real-Ephemeris Model of the Earth–Moon System*, pp. 33–59. Springer International Publishing, 2023, doi: 10.1007/978-3-031-24812-2.

[30] G. W. Hill, "Researches in the Lunar Theory," *American Journal of Mathematics*, Vol. 1, No. 1, 1878, pp. 5–26, doi: 10.2307/2369430.

[31] M. Hénon and J.-M. Petit, "Series expansions for encounter-type solutions of Hill's problem," *Celestial Mechanics*, Vol. 38, Jan. 1986, pp. 67–100, doi: 10.1007/bf01234287.

[32] S. Ichtiaroglou, "Elliptic Hill's problem: The continuation of periodic orbits," *Astronomy and Astrophysics*, Vol. 92, No. 1-2, 1980, pp. 139–141.

[33] G. W. Hill, "Researches in the Lunar Theory," *American Journal of Mathematics*, Vol. 1, No. 2, 1878, pp. 129–147, doi: 10.2307/2369304.

[34] G. W. Hill, "Researches in the Lunar Theory," *American Journal of Mathematics*, Vol. 1, No. 3, 1878, pp. 245–260, doi: 10.2307/2369313.

[35] M. Hénon, "Numerical Exploration of the Restricted Problem. V. Hill's case: Periodic orbits and their stability," *Astronomy and Astrophysics*, Vol. 1, 1969, pp. 223–238.

[36] G. M. Brown, L. T. Peterson, D. B. Henry, and D. J. Scheeres, "Structure of Periodic Orbit Families in the Hill Restricted 4-Body Problem," *SIAM Journal on Applied Dynamical Systems*, 2024. In Review, doi: 10.48550/ARXIV.2402.19181.

[37] Z. P. Olikara, G. Gómez, and J. J. Masdemont, *A Note on Dynamics About the Coherent Sun–Earth–Moon Collinear Libration Points*, pp. 183–192. Springer International Publishing, 2016.

[38] L. T. Peterson, J. J. Rosales, and D. J. Scheeres, "The vicinity of Earth–Moon L1 and L2 in the Hill restricted 4-body problem," *Physica D: Nonlinear Phenomena*, Vol. 455, Dec. 2023, p. 133889, doi: 10.1016/j.physd.2023.133889.

[39] L. T. Peterson, G. Brown, Á. Jorba, and D. Scheeres, "Dynamics around the Earth–Moon triangular points in the Hill restricted 4-body problem," *Celestial Mechanics and Dynamical Astronomy*, Vol. 136, July 2024, doi: 10.1007/s10569-024-10203-5.

[40] R. R. Sanaga and K. Howell, "Analyzing the Challenging Region in the Earth-Moon L2 Halo Family via Hill Restricted Four-Body Problem Dynamics," *AIAA SCITECH 2024 Forum*, American Institute of Aeronautics and Astronautics, 2024.

[41] R. R. Sanaga and K. C. Howell, "Leveraging the Hill restricted four-body problem to investigate the ephemeris transition characteristics in the Earth-Moon L2 halo orbit region," *Astrodynamics*, Vol. 9, Oct. 2025, pp. 785–805, doi: 10.1007/s42064-024-0250-4.

[42] E. J. Dennis, D. B. Henry, and D. J. Scheeres, "Exploring Higher-Dimensional Quasi-Periodic Orbits in the Hill Restricted Four-Body Problem," *AAS/AIAA Space Flight Mechanics Meeting*, Kauai, Hawaii, USA, 2025.

[43] E. W. Brown, *An Introductory Treatise on the Lunar Theory*. Cambridge: Cambridge University Press, 1896.

[44] N. Baresi, *Spacecraft Formation Flight on Quasi-periodic Invariant Tori*. phdthesis, University of Colorado Boulder, 2017.

[45] B. McCarthy, *Cislunar Trajectory Design Methodologies Incorporating Quasi-Periodic Structures with Applications*. phdthesis, Purdue University, 2022.

[46] D. A. Lujan, *Methods to Explore Families of Quasi-Periodic Orbits with Applications in Astrodynamics*. phdthesis, University of Colorado Boulder, 2023.

[47] D. B. Henry, *Spacecraft Trajectory Design and Control Leveraging Quasi-periodic Orbits*. phdthesis, University of Colorado Boulder, 2024.

[48] E. J. Doedel, R. C. Paffenroth, H. B. Keller, D. J. Dichmann, J. Galán-Vioque, and A. Vanderbauwhede, "Computation of Periodic Solutions of Conservative Systems with Application to the 3-Body Problem," *International Journal of Bifurcation and Chaos*, Vol. 13, June 2003, pp. 1353–1381, doi: 10.1142/s0218127403007291.

[49] F. Muñoz-Almaraz, E. Freire, J. Galán, E. Doedel, and A. Vanderbauwhede, "Continuation of periodic orbits in conservative and Hamiltonian systems," *Physica D: Nonlinear Phenomena*, Vol. 181, July 2003, pp. 1–38, doi: 10.1016/s0167-2789(03)00097-6.

[50] X. Fu, N. Baresi, and R. Armellin, "Numerical continuation and stationkeeping of quasi-periodic quasi-satellite orbits," *Acta Astronautica*, Vol. 238, Jan. 2026, pp. 997–1014, doi: 10.1016/j.actaastro.2025.09.065.

[51] C. Canuto, M. Y. Hussaini, A. Quarteroni, and T. A. Zang, *Spectral Methods: Fundamentals in Single Domains*. Springer Berlin Heidelberg, 2006, doi: 10.1007/978-3-540-30726-6.

[52] M. A. Patterson and A. V. Rao, "Exploiting Sparsity in Direct Collocation Pseudospectral Methods for Solving Optimal Control Problems," *Journal of Spacecraft and Rockets*, Vol. 49, Mar. 2012, pp. 354–377, 10.2514/1.a32071.

[53] D. Garg, M. Patterson, W. W. Hager, A. V. Rao, D. A. Benson, and G. T. Huntington, "A unified framework for the numerical solution of optimal control problems using pseudospectral methods," *Automatica*, Vol. 46, Nov. 2010, pp. 1843–1851, doi: 10.1016/j.automatica.2010.06.048.

[54] R. Seydel, *Practical Bifurcation and Stability Analysis*. Springer New York, 2010, doi: 10.1007/978-1-4419-1740-9.

[55] C. Aydin, "The Conley–Zehnder indices of the spatial Hill three-body problem," *Celestial Mechanics and Dynamical Astronomy*, Vol. 135, No. 3, 2023, p. 32, doi: 10.1007/s10569-023-10134-7.

APPENDIX A: HILL'S EQUATIONS OF MOTION AND JACOBI CONSTANT

The equations of motion of the third body in the nondimensional Hill's frame are obtained by applying the time and length scalings introduced in the main text. Using the nondimensional relative position of the Moon with respect to the Earth, $\boldsymbol{\rho}_{\mathrm{EM}} = \xi\hat{\mathbf{i}}_{\mathcal{H}} + \eta\hat{\mathbf{j}}_{\mathcal{H}} + \zeta\hat{\mathbf{k}}_{\mathcal{H}}$, the dynamics is governed by

$$\begin{cases} \overset{\star\star}{\xi} - 2\overset{\star}{\eta} = 3\xi - \dfrac{\xi}{\left(\xi^2+\eta^2+\zeta^2\right)^{3/2}} \\ \overset{\star\star}{\eta} + 2\overset{\star}{\xi} = -\dfrac{\eta}{\left(\xi^2+\eta^2+\zeta^2\right)^{3/2}} \\ \overset{\star\star}{\zeta} = -\zeta - \dfrac{\zeta}{\left(\xi^2+\eta^2+\zeta^2\right)^{3/2}} \end{cases}. \tag{33}$$

The system is an autonomous three-degree-of-freedom Hamiltonian system and admits the Jacobi constant

$$C_{\mathcal{H}} = \frac{1}{2}\left(\overset{\star}{\xi}^2 + \overset{\star}{\eta}^2 + \overset{\star}{\zeta}^2\right) - \frac{3}{2}\xi^2 + \frac{1}{2}\zeta^2 - \frac{1}{\sqrt{\xi^2+\eta^2+\zeta^2}}. \tag{34}$$

APPENDIX B: HR4BP EQUATIONS OF MOTION

The equations of motion of the HR4BP are given by[8]

$$\mathring{\mathbf{x}} = \mathbf{f}(\mathbf{x}, t_{\mathcal{S}}) := \begin{bmatrix} \mathbf{v} \\ \dfrac{\partial V}{\partial \mathbf{r}}(\mathbf{r}, t_{\mathcal{S}}) + 2(1+m)\,\mathbf{v}\times\hat{\mathbf{k}}_{\mathcal{S}} \end{bmatrix}, \tag{35}$$

where the time-periodic effective potential is

$$\begin{aligned} V(\mathbf{r}, t_{\mathcal{S}}) := &\frac{1}{2}\left(1 + 2m + \frac{3}{2}m^2\right)\left(x^2+y^2\right) - \frac{1}{2}m^2 z^2 \\ &+ \frac{3}{4}m^2\left(\left(x^2-y^2\right)\cos(2t_{\mathcal{S}}) - 2xy\sin(2t_{\mathcal{S}})\right) \\ &+ \frac{m^2}{a_0(m)^3}\left(\frac{1-\mu_{\mathrm{M,B}}}{\|\mathbf{r}-\mathbf{r}_{\mathrm{E}}(t_{\mathcal{S}})\|} + \frac{\mu_{\mathrm{M,B}}}{\|\mathbf{r}-\mathbf{r}_{\mathrm{M}}(t_{\mathcal{S}})\|}\right), \end{aligned} \tag{36}$$

and $\|\cdot\|$ denotes the Euclidean norm. The Hill variational orbit describing the relative Earth–Moon motion admits the following Fourier series representation:[23]

$$\mathbf{r}_{\mathrm{EM}}(t_{\mathcal{S}}) = \begin{bmatrix} 1 + \displaystyle\sum_{n=1}^{\infty}\left(\frac{a_n}{a_0}(m) + \frac{a_{-n}}{a_0}(m)\right)\cos(2nt_{\mathcal{S}}) \\ \displaystyle\sum_{n=1}^{\infty}\left(\frac{a_n}{a_0}(m) - \frac{a_{-n}}{a_0}(m)\right)\sin(2nt_{\mathcal{S}}) \\ 0 \end{bmatrix}. \tag{37}$$

In this work, the Fourier expansion is truncated after the $N = 9$ harmonic. The coefficients $a_i(m)$, for $i \in \{-N, \ldots, N\}$, are evaluated as functions of the parameter m using the polynomial approximations provided in Appendix A of Reference 36.

APPENDIX C: INITIAL MESH GENERATION

The adaptive collocation scheme requires an initial temporal discretization before the refinement procedure is applied. Although alternative initialization strategies (e.g., uniform discretizations in time, arclength, or accumulated linear momentum) are viable, the adaptive nature of the algorithm ensures that the initial mesh serves primarily as a starting guess, rather than dictating the final converged discretization. In this work, the initial mesh is dynamically tailored to the local behavior of a reference trajectory (e.g., a baseline periodic orbit).

Let $\mathbf{x}(t) = [\mathbf{r}(t)^\top, \mathbf{v}(t)^\top]^\top$, with $t \in [0, T]$, denote the reference trajectory. This orbit is first propagated using a sufficiently fine temporal discretization to generate a dense set of sampled states, $\{\mathbf{x}(t_i)\}_{i=1}^{N_\mathrm{g}}$, where N_g is chosen to be significantly larger than the initial prescribed number of collocation segments, K.

A temporal weight function, $w(t)$, is then evaluated along the trajectory to characterize the local dynamical timescale. In the present implementation, this function is defined as $w(t) = |\mathbf{v}(t)|/|\mathbf{r}(t) - \mathbf{r}_\mathrm{c}(t)|$, where $\mathbf{r}_\mathrm{c}(t)$ represents the position vector of the primary body of interest, i.e., the Moon. This formulation naturally clusters the grid points in regions where the spacecraft exhibits high velocity and close proximity to the primary, while allocating broader segments to dynamically smoother, distant portions of the trajectory.

This weight function is subsequently integrated to construct a normalized cumulative distribution function:

$$W(t) = \frac{\int_0^t w(\tau)\, d\tau}{\int_0^T w(\tau)\, d\tau}, \tag{38}$$

which strictly satisfies $W(0) = 0$ and $W(T) = 1$. The boundaries of the initial grid segments are determined by uniformly sampling this distribution; that is, by enforcing $W(t_k) = k/K$ for $k = 0, \ldots, K$. Because $W(t)$ is monotonically increasing, the grid times t_k are uniquely recovered via interpolation.

Finally, the resulting segment lengths, $\Delta t_k = t_{k+1} - t_k$, are linearly mapped onto the admissible range of polynomial degrees, $N_\mathrm{min} \leq N_k \leq N_\mathrm{max}$. Through this mapping, larger time segments are automatically assigned higher-order polynomials, whereas shorter segments employ lower-degree basis functions. The resulting set of pairs, $\{(t_k, N_k)\}_{k=1}^{K}$, provides the necessary parameters to construct the initial collocation mesh.

APPENDIX D: 3D INVARIANT SURFACES

While the complete three-dimensional invariant tori provide a global view of the quasi-periodic dynamics, their topological complexity can be difficult to fully interpret in a single projection onto $\mathbb{R}^3$. To further characterize these high-dimensional manifolds, this appendix details their two-dimensional invariant surfaces. By systematically fixing one of the three angular coordinates (θ_1, θ_2, or θ_3) and varying the remaining two, the resulting stroboscopic sections reveal the internal structure and the geometric evolution of the torus along each fundamental frequency. Specifically, the sections with a fixed θ_1 reveal the effect of the rotating frame, yielding stroboscopic surfaces that resemble the Moon's orbit (see Figure 13); fixing θ_2 displays the effect of the Sun's perturbation, while fixing θ_3 highlights the influence of the Earth-Moon eccentricity.

Figures 14, 15, 16, and 17 illustrate these invariant sections for QPOs belonging to the Halo, vertical Lyapunov, distant prograde orbit (DPO), and planar Lyapunov families, respectively. All surfaces are represented within the $\mathcal{S}$ frame, and the color mapping traces the progression of the fixed angle spanning the entire $[0, 2\pi]$ domain.

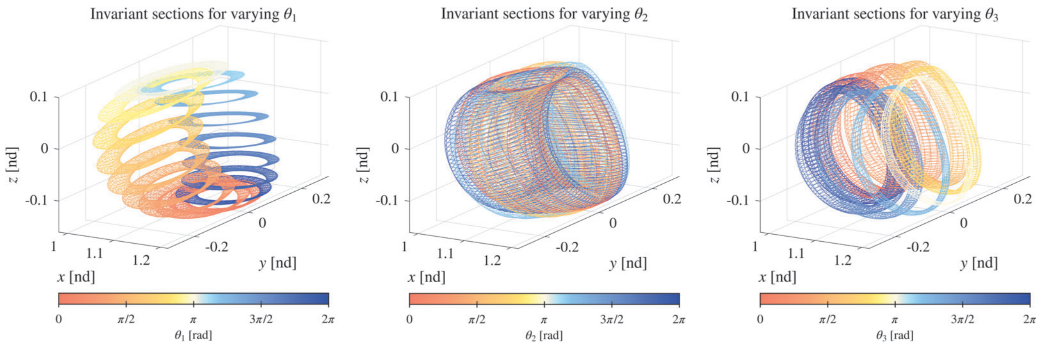

Figure 14. Invariant surfaces of a 3D L_2-Halo orbit in the IQHR4BP, $\mathcal{S}$ frame.

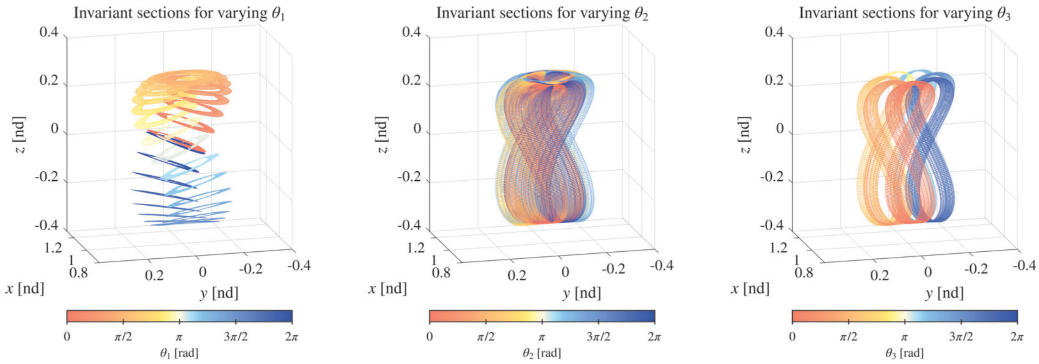

Figure 15. Invariant surfaces of a 3D L_2-Vertical orbit in the IQHR4BP, $\mathcal{S}$ frame.

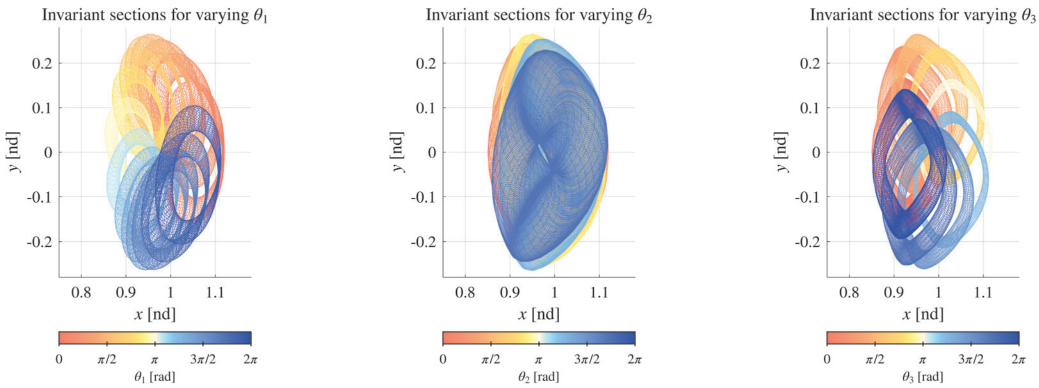

Figure 16. Invariant surfaces of a 3D DPO in the IQHR4BP, $\mathcal{S}$ frame.

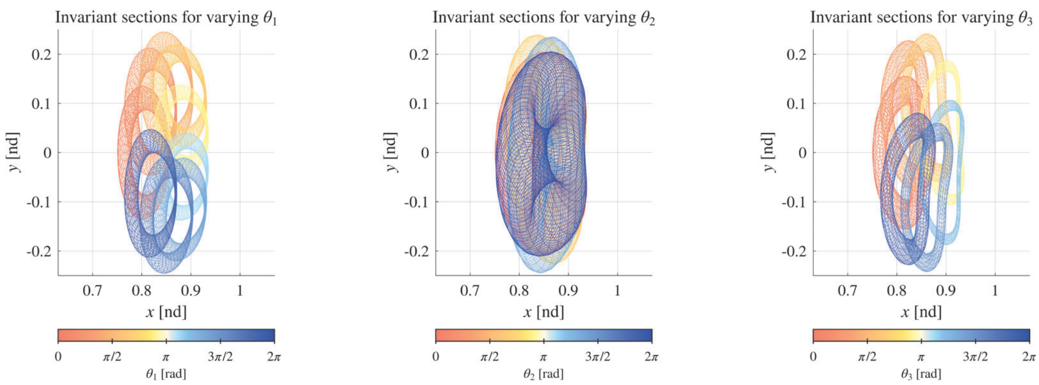

Figure 17. Invariant surfaces of a 3D L_1-Lyapunov orbit in the IQHR4BP, $\mathcal{S}$ frame.